

KAT6B overexpression rescues embryonic lethality in homozygous null KAT6A mice restoring vitality and normal lifespan

Received: 26 October 2023

Accepted: 10 February 2025

Published online: 25 February 2025

 Check for updates

Maria. I. Bergamasco ^{1,2}, Yuqing Yang^{1,2}, Alexandra L. Garnham^{1,2},
Bilal N. Sheikh ^{3,4}, Gordon K. Smyth ^{1,5}, Anne. K. Voss ^{1,2,6}  &
Tim Thomas ^{1,2,6} 

Closely related genes typically display common essential functions but also functional diversification, ensuring retention of both genes throughout evolution. The histone lysine acetyltransferases KAT6A (MOZ) and KAT6B (QKF/MORF), sharing identical protein domain structure, are mutually exclusive catalytic subunits of a multiprotein complex. Mutations in either *KAT6A* or *KAT6B* result in congenital intellectual disability disorders in human patients. In mice, loss of function of either gene results in distinct, severe phenotypic consequences. Here we show that, surprisingly, 4-fold overexpression of *Kat6b* rescues all previously described developmental defects in *Kat6a* mutant mice, including rescuing the absence of hematopoietic stem cells. *Kat6b* restores acetylation at histone H3 lysines 9 and 23 and reverses critical gene expression anomalies in *Kat6a* mutant mice. Our data suggest that the target gene specificity of KAT6A can be substituted by the related paralogue KAT6B, despite differences in amino acid sequence, if KAT6B is expressed at sufficiently high levels.

In eukaryotic cells, transcription is influenced by the nucleosomal barriers imposed by histone proteins. Post-translational modifications of chromatin, for example histone acetylation, regulate chromatin structure and influence the nucleosome landscape such as to promote or suppress the expression of target loci¹. Lysine acetylation is catalysed by acetyltransferase enzymes and generally associated with increased gene expression and the regulation of fundamental cellular functions^{2,3}. Three families of histone acetyltransferases, with well-described acetylation domains^{4,5}, are currently defined based on structural and sequence conservation: the MYST family⁶, the GNAT family⁷ and the p300/CBP family⁸.

Interestingly, histone lysine acetyltransferases typically occur as pairs of highly similar proteins. MYST family members KAT6A (MOZ) and KAT6B (QKF/MORF) share identical domain structure and high

sequence similarity across all functional domains⁶. Likewise, both the GNAT family proteins, KAT2A (GCN5) and KAT2B (PCAF)⁹ and the p300/CBP family proteins KAT3A (CBP) and KAT3B (P300)^{8,10,11} share identical domain structure and high sequence similarity across all functional domains. Sequence and structural similarities between family members likely resulted from ancestral gene duplication events and subsequent neofunctionalisation¹². Indeed, *in vivo* studies have demonstrated that these proteins have acquired independent functions^{13,14}; however, the extent to which one protein within a pair of closely related chromatin regulatory proteins can replace the other, has not been assessed.

KAT6A and KAT6B are mutually exclusive catalytic subunits of a shared multi-protein complex including chromatin adaptor proteins of the BRPF family, primarily BRPF1, ING family, ING5 and ING4, and

¹The Walter and Eliza Hall Institute of Medical Research, Parkville, VIC, Australia. ²Department of Medical Biology, The University of Melbourne, Parkville, VIC, Australia. ³Helmholtz Institute for Metabolic, Obesity and Vascular Research (HI-MAG) of the Helmholtz Center Munich, Leipzig, Germany. ⁴Medical Faculty, University of Leipzig, Leipzig, Germany. ⁵School of Mathematics and Statistics, University of Melbourne, Parkville, VIC, Australia. ⁶These authors contributed equally: Anne. K. Voss, Tim Thomas.  e-mail: avoss@wehi.edu.au; tthomas@wehi.edu.au

MEAF^{15,16}. Both proteins have been shown to acetylate H3K9 and H3K23 in a range of cell and tissue systems^{17–23}. The *KAT6A* and *KAT6B* genes are oncogenes. *KAT6A* (*MOZ*, monocytic leukaemia zinc finger gene) was originally identified in an aggressive form of acute myeloid leukaemia resulting from a translocation fusing it to *KAT3A*²⁴. A number of other recurrent translocations of the *KAT6A* locus have since been identified in leukaemia with a variety of translocation partners²⁵. Interestingly, loss of just one allele of *KAT6A* greatly enhances survival and disease latency in a mouse model of MYC driven lymphoma²⁶. Similarly, *KAT6B* translocations have been identified in leukaemia and leiomyomata^{27,28}. *KAT6A* and *KAT6B* mRNAs are commonly upregulated across a range of different cancer types²⁹. This association with cancer has fuelled the development of drugs targeting both *KAT6A* and *KAT6B* proteins^{30,31}, which have shown promise in clinical trials³².

In human patients, de novo mutations in *KAT6A* or *KAT6B* result in congenital disorders defined by cognitive impairment, developmental delay and craniofacial dysmorphogenesis^{33–36}. Heterozygous mutations in the *KAT6A* gene result in Arboleda-Tham syndrome (ARTHS)^{33,34}, while mutations in the *KAT6B* gene result in the Say-Barber-Biesecker-Young Simpson variant of Ohdo syndrome (SBBYSS)³⁵ or Genitopatellar syndrome (GPS)³⁶.

Deletion of the *Kat6a* or *Kat6b* gene in mice has identified their unique functions during development. Most *Kat6b*^{gt/gt} mice, deficient in 90% of *Kat6b* mRNA, die at birth on a 129 Sv inbred genetic background, while the 20% surviving *Kat6b*^{gt/gt} mice show a failure to thrive, short stature and a squared skull^{37,38}. *Kat6b*^{gt/gt} mice show abnormalities of the brain, including a reduced number of GAD67-positive interneurons and reduced numbers of layer V pyramidal neurons³⁷, as well as fewer neural stem cells (NSCs) in the adult subventricular zone. *Kat6b*^{gt/gt} NSCs show reduced proliferation and self-renewal and a reduced capacity to differentiate into neurons³⁹. Mice homozygous for a null allele of *Kat6b* show premature ossification and increased bone density in the skull and long bones⁴⁰. *Kat6b*^{+/-} show learning and memory defects that can be ameliorated by increasing histone acetylation⁴¹. These findings suggest that KAT6B function is primarily required for normal brain, craniofacial and skeletal development. Consistently, *Kat6b* is most strongly expressed in the primordia of these tissues during embryonic development³⁷.

Loss of KAT6A, either through deletion of the carboxy terminus or deletion of exons 5 to 9^{17,18}, results in lethality at embryonic day (E) 14–18, depending on the genetic background¹⁸, an absence of transplantable haematopoietic stem cells (HSCs)^{42,43}, an extensive anterior homeotic transformation¹⁷, cleft palate^{18,44} and cardiac and large vessel defects^{18,45}. The roles of KAT6A within the foetal haematopoietic system, have been shown to depend upon its histone acetyltransferase function^{46,47}. These tissues are not affected in mice lacking KAT6B, with the exception of a reduction, but not absence of hematopoietic stem cells in *Kat6b*^{-/-} embryos²³.

The recent development of drugs targeting both KAT6A and KAT6B has highlighted the need to better understand the cellular functions of these chromatin regulators. While it is clear from single knockout studies that one factor within the pair cannot compensate for the other at endogenous levels, it remains to be determined if there are truly unique, non-redundant functions of these proteins. To assess this, we overexpressed *Kat6b* mRNA 4-fold above endogenous levels in mice lacking *Kat6a*. We show here that *Kat6b* overexpression can restore all anomalies previously described in *Kat6a* mutant mice, including the 100% penetrant lethality, gene expression anomalies and histone acetylation deficits at histone lysine targets perturbed by loss of KAT6A. These data indicate that KAT6B can completely replace loss of essential KAT6A functions, if expressed at sufficiently high levels, despite KAT6B not normally regulating critical processes dependent on KAT6A.

Results

Structure and expression of KAT6A and KAT6B

KAT6A and *KAT6B* have identical protein domain structures and high sequence similarity in all functional domains (Fig. 1a). During development, *Kat6a* mRNA is expressed at higher levels than *Kat6b* mRNA (Fig. 1b). Heterozygous mutations in the human *KAT6A* gene result in ARTHS^{33,34}, while mutations in the *KAT6B* gene result in the Say-Barber-Biesecker-Young-Simpson variant of Ohdo syndrome (SBBYSS)³⁵ or genitopatellar syndrome (GTPS)³⁶. Despite being clinically distinct, there is notable overlap in the clinical presentation across these disorders (Supplementary Fig. 1b; Supplementary Data 1).

To test if transgenic overexpression of the *Kat6b* gene was able to rescue the phenotypic anomalies resulting from loss of the *Kat6a* gene, we generated transgenic mice overexpressing the *Kat6b* gene from *pBACe3.6* clone *RP23-36OF23*. This clone contained all coding exons as well as 21 kb 5 prime and 42 kb 3 prime of the expressed sequence (Supplementary Fig. 1a, b). Seven copies of the *pBACe3.6* inserted into the mouse genome, resulting in the *Tg(Kat6b)* allele, which caused a 4-fold increase in *Kat6b* mRNA levels (Supplementary Fig. 1c). Mice were maintained on an FVB x BALB/c hybrid background as *Kat6b* overexpressing mice were not viable on inbred backgrounds.

To assess the potential of KAT6B to compensate for KAT6A, we crossed *Tg(Kat6b)* heterozygous mice to mice lacking exons 5–9 of *Kat6a* (*Kat6a*^{+/-})^{17,18}. Embryonic day (E) 9.5 *Tg(Kat6b)* embryos and E14.5 and E18.5, *Tg(Kat6b)* foetuses were present at expected Mendelian ratios ($N=15$, $p=0.2$; $N=21$, $p=0.6$; $N=18$, $p=0.6$; at E9.5, E14.5 and E18.5, respectively; binomial probability p values). *Kat6a*^{-/-} foetuses were underrepresented at E18.5 ($N=16$, $p=0.8$; $N=6$, $p=0.1$; $N=4$, $p=0.02$; at E9.5, E14.5 and E18.5, respectively). In contrast, *Kat6a*^{-/-}*Tg(Kat6b)* foetuses that lacked *Kat6a*, but overexpressed *Kat6b*, were obtained at the expected Mendelian ratio ($N=9$, $p=1.0$; $N=8$, $p=1.0$; $N=10$, $p=1.0$; at E9.5, E14.5 and E18.5, respectively).

Kat6b overexpression restored histone acetylation and cell proliferation in *Kat6a*^{-/-}*Tg(Kat6b)* fibroblasts and histone acetylation in *Kat6a*^{-/-}*Tg(Kat6b)* embryos

To determine whether KAT6B was capable of compensating for the loss of KAT6A at the biochemical level, histone acetylation levels at previously identified KAT6A lysine targets, H3K9 and H3K23, as well as H3K14, were assessed chromatin-wide by Western blotting in primary mouse embryonic fibroblasts (MEFs) and in whole embryonic day 9.5 (E9.5) embryos.

Kat6a^{-/-} MEFs had a 40% reduction in acetylation at H3K23 (H3K23ac), relative to wild type controls ($p=0.03$; Fig. 1c, d). Overexpression of *Kat6b* in *Kat6a*^{-/-}*Tg(Kat6b)* MEFs returned H3K23ac levels to wild-type levels (Fig. 1c, d). H3K23ac was similar in *Kat6b*^{+/-}*Tg(Kat6b)* and wild-type *Kat6a*^{+/-}*Kat6b*^{+/-} control MEFs (Fig. 1c, d). Chromatin-wide H3K9 and H3K14 acetylation levels were not affected by KAT6A or KAT6B status in this cell type (Supplementary Fig. 2a–d).

Consistent with previous reports^{30,47,48}, *Kat6a*^{-/-}*Kat6b*^{+/-} MEFs underwent cell cycle arrest after only 3 passages in culture ($p=0.00007$; Fig. 1e, f). Overexpression of *Kat6b* restored cell proliferation in *Kat6a*^{-/-}*Tg(Kat6b)* MEFs compared to *Kat6a*^{-/-}*Kat6b*^{+/-} cells to levels similar to wild-type *Kat6a*^{+/-}*Kat6b*^{+/-} control MEFs (Fig. 1e, f).

In E9.5 *Kat6a*^{-/-}*Kat6b*^{+/-} embryos, acetylation levels at H3K9 ($p=0.046$; Fig. 1g, h) and H3K23 ($p=0.02$; Fig. 1i, j) were 32% and 43% reduced, respectively, compared to *Kat6a*^{+/-}*Kat6b*^{+/-} control embryos. Overexpression of *Kat6b* returned the histone acetylation levels to normal in *Kat6a*^{-/-}*Tg(Kat6b)* embryos compared to *Kat6a*^{+/-}*Kat6b*^{+/-} control embryos (Fig. 1c, d, g–j). Interestingly, H3K9 and H3K23 were elevated by 41% and 39%, respectively, in *Kat6a*^{+/-}*Tg(Kat6b)* samples compared to controls ($p=0.01–0.03$); (Fig. 1g–j). H3K14ac was not affected by KAT6A or KAT6B status in E9.5 embryos (Supplementary

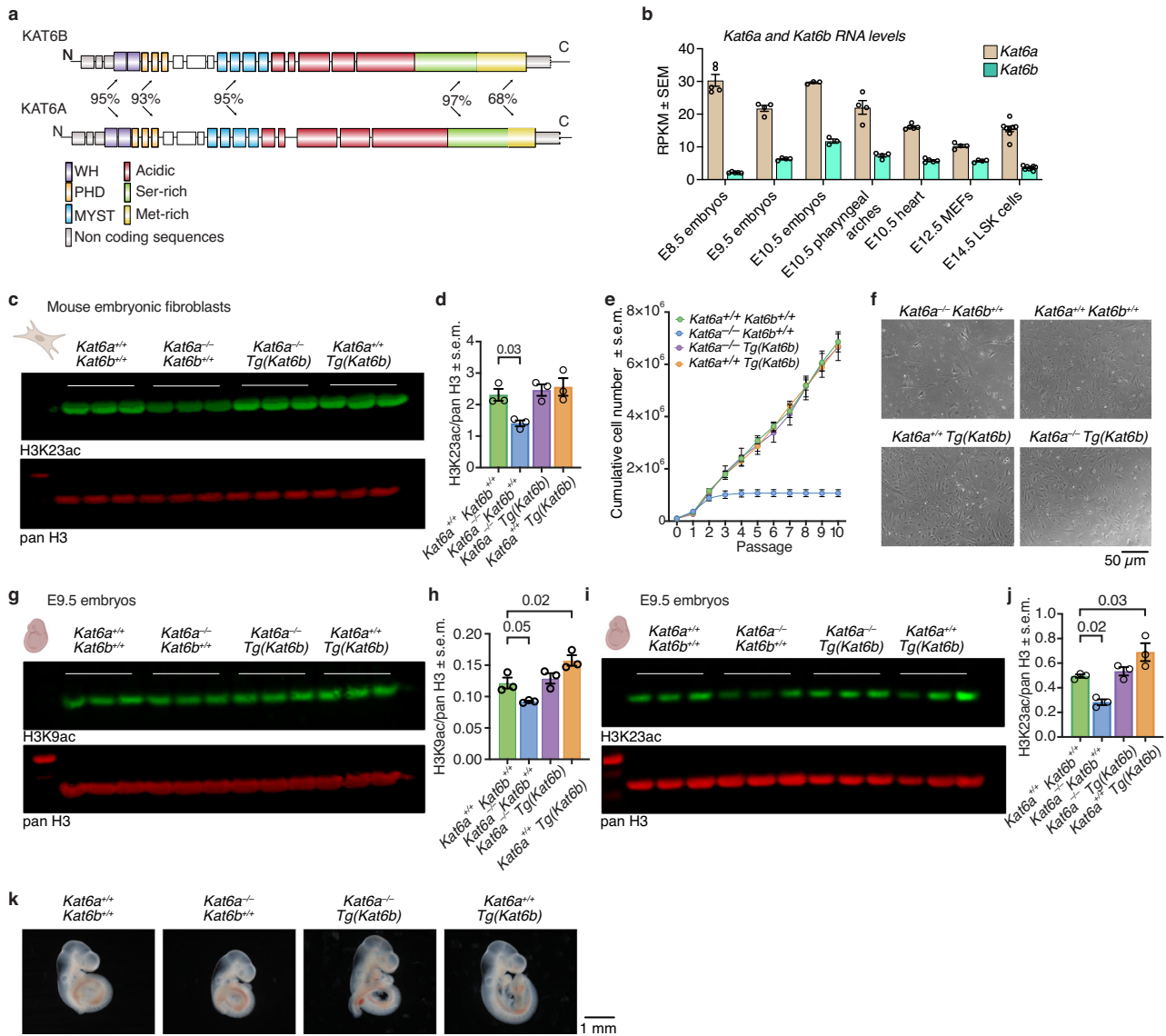


Fig. 1 *Kat6b* overexpression restores histone acetylation and cell proliferation in *Kat6a*^{-/-} *Tg(Kat6b)* fibroblasts and histone acetylation in *Kat6a*^{-/-} *Tg(Kat6b)* embryos. **a** Schematic of *KAT6A* and *KAT6B* mRNA with exon structure and protein domains/regions encoded are shown in colour. White boxes indicate an uncharacterised region. The percentage amino acid sequence similarity between protein domains is indicated. Non-coding exons are indicated in grey. **b** *Kat6a* and *Kat6b* mRNA levels from RNA-seq experiments analysing E8.5 embryos⁷⁵, E9.5 embryos (this work), E10.5 embryos⁵⁴, E10.5 pharyngeal arches⁴⁴, E10.5 heart⁷⁵, E12.5 MEFs⁶⁹, E14.5 LSK cells⁷⁶. **c** Western immunoblot detecting histone H3 acetylated on lysine 23 (H3K23ac) and pan-H3 as a loading control in acid extracted histones from E14.5 mouse embryonic fibroblasts (MEFs). Each lane represents histones from MEFs isolated from an individual E14.5 foetus. 250 ng protein loaded per lane. **d** Quantification of the western immunoblot in (a). Each circle represents one lane of the immunoblot in (a). **e** Cumulative growth curve of MEFs isolated from *Kat6a*^{+/+}*Kat6b*^{+/+}, *Kat6a*^{-/-}*Kat6b*^{+/+}, *Kat6a*^{+/+}*Tg(Kat6b)* and *Kat6a*^{-/-}*Tg(Kat6b)* E14.5

foetuses, passages 0–10. **f** Representative images of MEFs from *Kat6a*^{+/+}*Kat6b*^{+/+}, *Kat6a*^{-/-}*Kat6b*^{+/+}, *Kat6a*^{+/+}*Tg(Kat6b)* and *Kat6a*^{-/-}*Tg(Kat6b)* E14.5 foetuses at passage 3. Scale bar = 50 μ m. **g–j** Western immunoblot detecting H3K9ac (e) and H3K23ac (g) with pan-H3 as a loading on acid extracted histones from E9.5 embryos. Each lane represents histones from an individual E9.5 embryo. 500 ng (g) or 250 ng (i) protein loaded per lane. Quantification of (g) in (h) and of (i) in (j). **k** Representative images of E9.5 *Kat6b*^{+/+}*Kat6b*^{+/+}, *Kat6a*^{-/-}*Kat6b*^{+/+}, *Kat6a*^{-/-}*Tg(Kat6b)* and *Kat6a*^{+/+}*Tg(Kat6b)* embryos. Scale bar = 1 mm. *N* = 3–8 embryos or foetuses per genotype (a), MEF cultures derived from 3 foetuses per genotype (c, d, e, f). 3 embryos per genotype (g, h, i, j, k). Circles represent individual embryos or foetuses (b, d, h, j). Data are presented as mean \pm s.e.m. and were analysed using a one-way ANOVA with Dunnett post hoc correction (b, g, i) or two-way ANOVA with Sidak post-hoc correction (c). Drawings created in BioRender, Bergamasco, M. (2025) <https://BioRender.com/m13f247>.

Fig. 2e, f). Representative images of E9.5 embryos are shown in (Fig. 1k).

***Kat6b* overexpression reversed most gene expression changes present in *Kat6a*^{-/-} E9.5 embryos**

Loss of KAT6A has previously been shown to reduce expression of gene families encoding embryonic patterning transcription factors, most notably *Hox* genes¹⁷, *Tbx* genes¹⁸ and *Dlx* genes⁴⁴. To determine how

mRNA levels affected by loss of KAT6A were altered when KAT6B was overexpressed, we performed RNA-sequencing of *Kat6a*^{-/-}*Kat6b*^{+/+}, *Kat6a*^{+/+}*Kat6b*^{+/+}, *Kat6a*^{-/-}*Tg(Kat6b)* and *Kat6a*^{+/+}*Tg(Kat6b)* E9.5 embryos (Supplementary Data 2–5). E9.5 was chosen as a timepoint when major patterning genes previously shown to be perturbed by loss of KAT6A are highly expressed.

Samples clustered within genotype and segregated between genotypes (Fig. 2a). Interestingly, *Kat6a*^{-/-}*Tg(Kat6b)* RNA profiles were

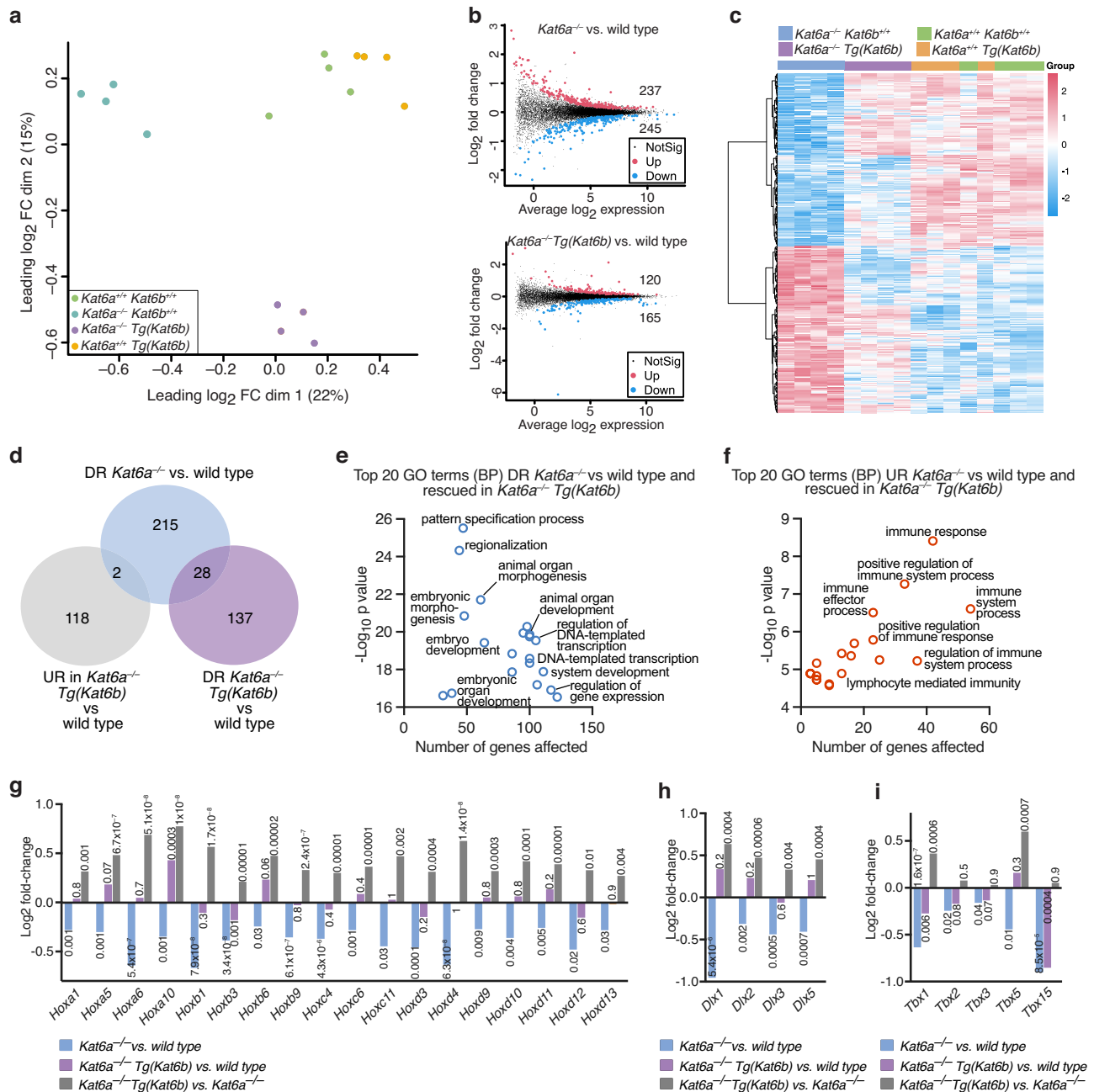


Fig. 2 | *Kat6b* overexpression reverses gene expression changes present in *Kat6a*^{-/-} E9.5 embryos. **a–i RNA-sequencing data of *Kat6a*^{+/+}*Kat6b*^{+/+}, *Kat6a*^{-/-}*Kat6b*^{+/+}, *Kat6a*^{-/-}*Tg(Kat6b)* and *Kat6a*^{+/+}*Tg(Kat6b)* E9.5 embryos. *N* = 4 embryos per genotype. Data were analysed as described in the ‘methods’ section. A false discovery (FDR) < 0.05 was used as the cut off for significance. **a** Multidimensional scaling plot of the leading gene expression differences between samples in pair-wise comparisons showing *Kat6a*^{+/+}*Kat6b*^{+/+}, *Kat6a*^{-/-}*Kat6b*^{+/+}, *Kat6a*^{-/-}*Tg(Kat6b)* and *Kat6a*^{+/+}*Tg(Kat6b)* E9.5 embryo RNA samples. **b** M (log ratio) and A (mean average) plot showing *Kat6a*^{-/-}*Kat6b*^{+/+} vs. *Kat6a*^{+/+}*Kat6b*^{+/+} and *Kat6a*^{-/-}*Tg(Kat6b)* vs. *Kat6a*^{+/+}*Kat6b*^{+/+} embryos. The total numbers of upregulated and downregulated genes at FDR < 0.05 are indicated in each comparison. Upregulated genes are represented in red, downregulated in blue and unchanged genes in grey. **c** Heatmap showing genes differentially expressed in the contrast of *Kat6a*^{-/-}*Kat6b*^{+/+} vs. *Kat6a*^{+/+}*Kat6b*^{+/+} embryos but displayed for all genotypes. **d** Venn diagram showing the intersection of genes downregulated (DR) in *Kat6a*^{-/-} *Kat6b*^{+/+} vs. *Kat6a*^{+/+}*Kat6b*^{+/+} embryos with those**

downregulated in *Kat6a*^{-/-}*Tg(Kat6b)* samples vs. *Kat6a*^{+/+}*Kat6b*^{+/+} embryos compared to those upregulated in *Kat6a*^{-/-}*Tg(Kat6b)* samples vs. *Kat6a*^{+/+}*Kat6b*^{+/+} embryos. **e** Top 20 gene ontology (GO) (BP) terms downregulated in *Kat6a*^{-/-}*Kat6b*^{+/+} vs. *Kat6a*^{+/+}*Kat6b*^{+/+} embryos and rescued in *Kat6a*^{-/-}*Tg(Kat6b)* when compared to *Kat6a*^{+/+}*Kat6b*^{+/+} embryos. GO terms enriched with *p* < 10⁻⁶ are shown. **f** Top 20 gene ontology (GO) (BP) terms upregulated in *Kat6a*^{-/-}*Kat6b*^{+/+} vs. *Kat6a*^{+/+}*Kat6b*^{+/+} embryos and rescued in *Kat6a*^{-/-}*Tg(Kat6b)* when compared to *Kat6a*^{+/+}*Kat6b*^{+/+} embryos. GO terms enriched with *p* < 10⁻⁶ are shown. **g–i** Specific gene families previously reported to be affected by loss of KAT6A^{27,38,44} were examined. Correction for multiple testing was conducted within gene family. FDRs for each comparison are shown above each bar. **g–i** Log₂ fold-change in levels of HOX gene mRNA (**g**), DLX gene mRNA (**h**) and TBX gene mRNA (**i**) across pairwise comparisons *Kat6a*^{-/-}*Kat6b*^{+/+} vs. *Kat6a*^{+/+}*Kat6b*^{+/+} embryos, *Kat6a*^{-/-}*Tg(Kat6b)* vs. *Kat6a*^{+/+}*Kat6b*^{+/+} embryos and *Kat6a*^{-/-}*Tg(Kat6b)* vs. *Kat6a*^{-/-}*Kat6b*^{+/+} embryos. FDRs are displayed above or below the bars.

more closely related to wild-type control profiles in dimension 1, as assessed by multidimensional scaling, compared to *Kat6a*^{-/-}*Kat6b*^{+/+} profiles, but segregated from the other genotypes in dimension 2, indicating that, despite more closely resembling wild-type controls than *Kat6a*^{-/-}*Kat6b*^{+/+} samples, *Kat6a*^{-/-}*Tg(Kat6b)* samples still maintained distinct RNA expression profiles.

A total of 482 genes were differentially expressed in *Kat6a*^{-/-}*Kat6b*^{+/+} vs. *Kat6a*^{+/+}*Kat6b*^{+/+} E9.5 embryos with transcriptome-wide significance (FDR < 0.05); 245 genes were downregulated, and 237 genes were upregulated (Supplementary Data 2). Overexpression of *Kat6b* in *Kat6a*^{-/-}*Tg(Kat6b)* embryos reduced the number of differentially expressed genes compared to *Kat6a*^{+/+}*Kat6b*^{+/+} embryos to 285 genes, 165 downregulated and 120 upregulated (Fig. 2b; Supplementary Data 3). Other pairwise comparisons are shown in Supplementary Fig. 3a and Supplementary Data 4–7. A heat map shows that *Kat6a*^{-/-}*Tg(Kat6b)* embryos clustered more closely with wild-type *Kat6a*^{+/+}*Kat6b*^{+/+} control embryos than *Kat6a*^{-/-}*Kat6b*^{+/+} samples (Fig. 2c).

Of the 245 genes downregulated in *Kat6a*^{-/-}*Kat6b*^{+/+} vs. *Kat6a*^{+/+}*Kat6b*^{+/+}, only 28 genes were similarly downregulated in *Kat6a*^{-/-}*Tg(Kat6b)* samples (Fig. 2d; Supplementary Data 2 and 3), while two of the rescued genes, (*Cdx2*, *Hoxa10*), were overcompensated, i.e., expressed at higher levels in *Kat6a*^{-/-}*Tg(Kat6b)* vs. *Kat6a*^{+/+}*Kat6b*^{+/+} E9.5 embryos.

The genes downregulated in *Kat6a*^{-/-}*Kat6b*^{+/+} vs. *Kat6a*^{+/+}*Kat6b*^{+/+} E9.5 embryos were enriched in gene ontology (BP) terms relating to embryonic development, embryo patterning and DNA binding transcription factors regulating these processes (Supplementary Fig. 3b). The genes that displayed a rescue of mRNA levels from downregulated in *Kat6a*^{-/-}*Kat6b*^{+/+} vs. *Kat6a*^{+/+}*Kat6b*^{+/+} E9.5 embryos to normal levels in *Kat6a*^{-/-}*Tg(Kat6b)* vs. *Kat6a*^{+/+}*Kat6b*^{+/+} E9.5 embryos were enriched for similar developmental processes (Fig. 2e, f). Genes upregulated in *Kat6a*^{-/-}*Kat6b*^{+/+} vs. *Kat6a*^{+/+}*Kat6b*^{+/+} E9.5 embryos showed no specificity to embryonic development (Supplementary Fig. 3c).

Among the rescued genes were the major families of embryonic patterning genes previously reported as downregulated in *Kat6a*^{-/-} vs. *Kat6a*^{+/+} embryos; *Hox* genes¹⁷, *Tbx* genes¹⁸ and *Dlx* genes⁴⁴. The major downregulation of *Hox* genes observed in *Kat6a*^{-/-}*Kat6b*^{+/+} vs. *Kat6a*^{+/+}*Kat6b*^{+/+} E9.5 embryos (FDR < 10⁻⁶ to 0.03 within gene family; Supplementary Fig. 3d, e; Data 8) was no longer present in *Kat6a*^{-/-}*Tg(Kat6b)* vs. *Kat6a*^{+/+}*Kat6b*^{+/+} E9.5 embryos (Fig. 2g), indicating that KAT6B can promote expression of *Hox* genes in the absence of KAT6A. Only *Hoxb3* mRNA levels were not fully returned to wild-type levels, but still were significantly elevated in *Kat6a*^{-/-}*Tg(Kat6b)* vs. *Kat6a*^{-/-}*Kat6b*^{+/+} embryos (FDR = 10⁻⁵; Fig. 2g), indicating a partial rescue. Similarly, *Dlx* genes downregulated in *Kat6a*^{-/-}*Kat6b*^{+/+} vs. *Kat6a*^{+/+}*Kat6b*^{+/+} embryos (FDR = 6 × 10⁻⁵ to 0.004 within gene family; Supplementary Fig. 3d, e, Data 8) were no longer downregulated in *Kat6a*^{-/-}*Tg(Kat6b)* vs. *Kat6a*^{+/+}*Kat6b*^{+/+} (FDR = 0.2 to 1; Fig. 2h). *Tbx* genes were downregulated in *Kat6a*^{-/-}*Kat6b*^{+/+} vs. *Kat6a*^{+/+}*Kat6b*^{+/+} embryos (FDR < 10⁻⁶ to 0.04 within gene family; Supplementary Data 8) and were upregulated in *Kat6a*^{-/-}*Tg(Kat6b)* vs. *Kat6a*^{-/-}*Kat6b*^{+/+}, except *Tbx15* (Fig. 2i; Supplementary Fig. 3d, e, Supplementary Data 8). This upregulation returned *Tbx2*, *Tbx3* and *Tbx5* mRNA levels in *Kat6a*^{-/-}*Tg(Kat6b)* embryos to comparable levels to *Kat6a*^{+/+}*Kat6b*^{+/+} embryos (FDR = 0.06 to 0.3). The mRNA levels of *Tbx1* were significantly elevated in *Kat6a*^{-/-}*Tg(Kat6b)* embryos above *Kat6a*^{-/-}*Kat6b*^{+/+} embryos (FDR = 0.0006), but still lower than in *Kat6a*^{+/+}*Kat6b*^{+/+} embryos (FDR = 0.006), indicating a partial rescue. Overall, 217 (89%) of 245 genes downregulated and 222 (94%) of the 237 upregulated genes in *Kat6a*^{-/-}*Kat6b*^{+/+} vs. *Kat6a*^{+/+}*Kat6b*^{+/+} E9.5 embryos were rescued by overexpression of *Kat6b* in *Kat6a*^{-/-}*Tg(Kat6b)* vs. *Kat6a*^{+/+}*Kat6b*^{+/+} embryos, indicating that KAT6B overexpression substantially restores expression of genes, which were reduced in the absence of KAT6A (Fig. 2d; Supplementary Fig. 4a, b). Examining the gene expression not

rescued in more detail we found the majority of these 28 downregulated and 15 upregulated genes showed relatively small differential gene expression changes, less than 2-fold, (Supplementary Fig. 4c, d), which were associated with GO terms relating to transcription in the case of downregulated genes and cell adhesion in the case of upregulated genes (Supplementary Fig. 4e, f). Some 236 genes were uniquely differentially expressed in *Kat6a*^{-/-}*Tg(Kat6b)* vs. *Kat6a*^{+/+}*Kat6b*^{+/+} embryos (Supplementary Fig. 4g–i) and a comparatively small number of genes (75) were differentially expressed when embryos overexpressing *Kat6b* were compared to wild type (Supplementary Fig. 4j–l).

***Kat6b* overexpression restored transplantable haematopoietic stem cells that are absent in *Kat6a*^{-/-} mice**

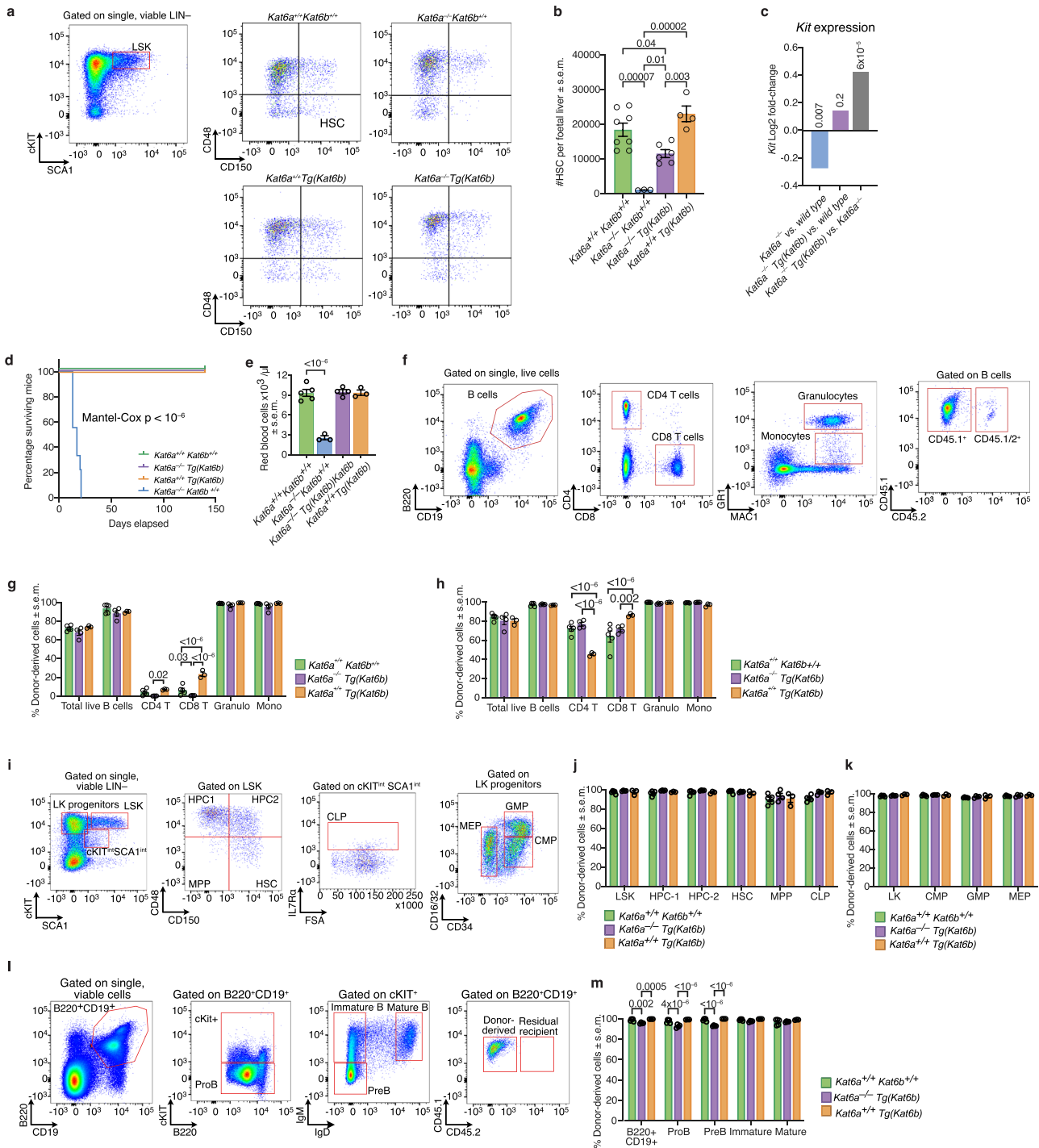
KAT6A is essential for development of HSCs. Germline deletion of the *Kat6a* gene results in a complete failure to form definitive HSCs during foetal development^{42,43}, and deletion of *Kat6a* in adult HSCs causes their complete loss⁴⁹.

The numbers of HSCs in *Kat6a*^{+/+}*Kat6b*^{+/+}, *Kat6a*^{+/+}*Tg(Kat6b)*, *Kat6a*^{-/-}*Kat6b*^{+/+} and *Kat6a*^{-/-}*Tg(Kat6b)* foetal livers were assessed by flow cytometry (Fig. 3a, b). Analysis was performed at E14.5, at the peak of foetal haematopoiesis in mice^{50,51} and HSCs were identified as CD48⁻CD150⁺, as described⁵². As previously described^{42,43}, *Kat6a*^{-/-}*Kat6b*^{+/+} foetal livers showed a 95% reduction in cells with an HSC cell surface phenotype compared to wild-type *Kat6a*^{+/+}*Kat6b*^{+/+} control foetal livers ($p = 0.00007$; Fig. 3b). Overexpression of *Kat6b* in *Kat6a*^{-/-}*Tg(Kat6b)* foetuses elevated the number of HSC 11.5-fold, compared to *Kat6a*^{-/-}*Kat6b*^{+/+} foetuses ($p = 0.01$; Fig. 3b), however, HSCs were still reduced in *Kat6a*^{-/-}*Tg(Kat6b)* foetuses compared to *Kat6a*^{+/+}*Kat6b*^{+/+} control foetuses ($p = 0.04$; Fig. 3b). Consistently, expression of the haematopoietic marker gene *Kit*^{50,53} was downregulated in *Kat6a*^{-/-}*Kat6b*^{+/+} vs. *Kat6a*^{+/+}*Kat6b*^{+/+} E9.5 embryos (FDR = 0.007; Fig. 3c), rescued in *Kat6a*^{-/-}*Tg(Kat6b)* vs. wild-type embryos (FDR = 0.2) and upregulated in *Kat6a*^{-/-}*Tg(Kat6b)* vs. *Kat6a*^{-/-}*Kat6b*^{+/+} embryos (FDR = 6 × 10⁻⁵; Fig. 3c).

To assess the effect of KAT6B overexpression on the function of HSCs lacking KAT6A, 1 × 10⁶ foetal liver cells were transplanted into irradiated recipients, as previously described⁴³. Recipients of *Kat6a*^{-/-}*Kat6b*^{+/+} foetal liver cells reached the ethical endpoint within 21 days ($p < 10^{-6}$; Fig. 3d), exhibiting anaemia ($p = 10^{-6}$; Fig. 3e) and minimal contribution of the foetal liver donor cells to the recipient peripheral blood (Supplementary Fig. 5a). In contrast, recipients of *Kat6a*^{-/-}*Tg(Kat6b)* cells survived beyond 150 days, as did recipients of wild type or *Kat6a*^{+/+}*Tg(Kat6b)* cells (Fig. 3d). At 4 weeks post-transplantation, *Kat6a*^{-/-}*Tg(Kat6b)* donor cell contribution to peripheral blood cells was similar to *Kat6a*^{+/+}*Kat6b*^{+/+} donor cells, except for a reduction in CD8 T cells ($p = 0.03$; Fig. 3f, g). At 20 weeks post-transplantation, contribution to all peripheral cell types was identical between *Kat6a*^{-/-}*Tg(Kat6b)* and *Kat6a*^{+/+}*Kat6b*^{+/+} donor cells (Fig. 3h). Interestingly, compared to wild type controls, *Kat6a*^{+/+}*Tg(Kat6b)* donor cells showed an elevated contribution to CD8 T cells at 4 weeks, ($p < 10^{-6}$; Fig. 3g) and 20 weeks ($p = 0.00005$; Fig. 3h), with a reduced contribution to CD4 T cells at 20 weeks ($p < 10^{-6}$; Fig. 3h). In the bone marrow at 20 weeks post-transplantation, recipients of *Kat6a*^{-/-}*Tg(Kat6b)*, *Kat6a*^{+/+}*Kat6b*^{+/+} and *Kat6a*^{+/+}*Tg(Kat6b)* donor cells showed comparable contributions to all stem and progenitor cell populations, except for a small reduction (less than 10%) in *Kat6a*^{-/-}*Tg(Kat6b)* contribution to the B220⁺CD19⁺, ProB and PreB cell populations ($p < 10^{-6}$ to 0.002; Fig. 3i–m). No difference was observed between recipients of *Kat6a*^{+/+}*Kat6b*^{+/+} and *Kat6b*^{+/+}*Tg(Kat6b)* recipients across bone marrow populations analysed (Fig. 3i–m).

***Kat6b* overexpression rescued the anterior homeotic transformation seen in *Kat6a*^{-/-} mice**

Germline deletion of the *Kat6a* gene results in duplication of the first cervical vertebra, the atlas, accompanied by an extensive and



complete homeotic transformation of 19 body segments. This anterior homeotic transformation is caused by a posterior shift of the anterior expression boundary and expression levels of *Hox* genes, including *Hoxa3*, *Hoxa4*, *Hoxb3* and *Hoxb4*¹⁷. Consistent with this previous work¹⁷ and the reduced *Hox* gene expression in E9.5 embryos shown here (Fig. 2g), *Kat6a*^{-/-} *Kat6b*^{+/-} pups displayed an anterior homeotic transformation at E18.5 (Fig. 4a; Supplementary Fig. 6). In addition, we saw disrupted sternum sections, sternbrae and incorrect alignment of ribs at the sternum in *Kat6a*^{-/-} *Kat6b*^{+/-} pups (Fig. 4b). Congruent with a rescue of the *Hox* gene expression profile at E9.5 (Fig. 2g), the vertebral segment identity, sternbrae structure and rib attachment were rescued in *Kat6a*^{-/-} *Tg(Kat6b)* pups at E18.5 (Fig. 4a, b). The cervical vertebrae, sternbrae and rib attachment were normal in *Kat6a*^{+/-} *Kat6b*^{+/-} and *Kat6a*^{+/-} *Tg(Kat6b)* pups (Fig. 5a, b). No obvious effects of KAT6A or

KAT6B genotype was observed on lumbar and sacral elements (Supplementary Fig. 7).

To examine the pattern of *Hox* gene expression more closely we performed whole mount in situ hybridisation. We have previously shown that not only is *Hox* gene expression down regulated in embryos but also that the anterior boundary is shifted posteriorly, which leads to an anterior homeotic transformation¹⁷. We examined the expression patterns of *Hoxa3*, *Hoxa5* and *Hoxc5*, as we have previously shown that the expression of these genes most clearly demonstrates the effect of *Kat6a* loss on the anterior boundary of *Hox* gene expression^{17,54}. As previously reported, the *Hoxa5* and *Hoxc5* expression is shifted posteriorly and expressed at lower levels in *Kat6a*^{-/-} *Kat6b*^{+/-} embryos (Fig. 4c, d; Supplementary Fig. 7). The anterior boundary and level of expression of both *Hoxa5* and *Hoxc5* in

Fig. 3 | *Kat6b* overexpression restores transplantable haematopoietic stem cells that are absent in *Kat6a*^{-/-} mice. **a** Flow cytometry gating strategy for the assessment of haematopoietic stem cells (HSCs) in E14.5 foetal livers. HSCs were identified as the CD48⁺CD150⁺ cell population within the lineage marker negative (LIN⁻) cKIT and SCA1 positive cell population (LSK; gated on single, viable cells, lacking expression of lineage (LIN) markers B220, CD19, CD4, CD8, GRI and TER119 and expressing SCA1 and cKIT). Representative plots for HSCs are shown for each genotype. **b** Total number of HSCs per foetal liver of $N = 3$ *Kat6a*^{-/-}*Kat6b*^{+/+}, $N = 8$ *Kat6a*^{+/+}*Kat6b*^{+/+}, $N = 6$ *Kat6a*^{-/-}*Tg(Kat6b)* and $N = 4$ *Kat6a*^{+/+}*Tg(Kat6b)* foetuses. **c** Log₂ fold-change in *Kit* mRNA levels in E9.5 embryos as assessed by RNA-sequencing across the comparisons *Kat6a*^{-/-}*Kat6b*^{+/+} vs. *Kat6a*^{+/+}*Kat6b*^{+/+}, *Kat6a*^{-/-}*Tg(Kat6b)* vs. *Kat6a*^{+/+}*Kat6b*^{+/+} and *Kat6a*^{-/-}*Tg(Kat6b)* vs. *Kat6a*^{-/-}*Kat6b*^{+/+} embryos. $N = 4$ embryos per genotype. The FDRs are shown above the bars. Data were analysed as described in the 'methods' section under *RNA sequencing and analysis*. **d** Percentage survival of irradiated recipient mice after transplantation of 1×10^6 foetal liver cells from $N = 3$ *Kat6a*^{-/-}*Kat6b*^{+/+}, $N = 4$ *Kat6a*^{-/-}*Tg(Kat6b)*, $N = 3$ *Kat6a*^{+/+}*Tg(Kat6b)* or $N = 5$ *Kat6a*^{+/+}*Kat6b*^{+/+} E14.5 mouse foetuses; each foetal liver sample was transplanted into 3 lethally irradiated recipients. Data are displayed in a Kaplan-Meier plot and were analysed using a Mantel-Cox test. **e** Automated haematological analyser (ADVIA) assessment of red blood cells per μ l peripheral blood in recipient mice of E14.5 foetal liver donor cells from $N = 5$ *Kat6a*^{+/+}*Kat6b*^{+/+}, $N = 3$ *Kat6a*^{-/-}*Tg(Kat6b)*, $N = 4$ *Kat6a*^{-/-}*Tg(Kat6b)* or $N = 3$ *Kat6a*^{-/-}*Kat6b*^{+/+} foetuses, at a time 3–4 weeks after transplantation when the recipient mice of *Kat6a*^{-/-}*Kat6b*^{+/+} donor cells in each set reached the ethical end-point. Each foetal liver sample was transplanted into 3 recipient mice. Each circle represents the average of the recipient mice of an individual foetal liver donor. Data are displayed as mean \pm s.e.m. and were analysed using a one-way ANOVA with Dunnett post-hoc correction.

f Gating strategy for the assessment of peripheral blood of foetal liver transplant recipient mice. B cells were defined as B220⁺CD19⁺, T cells as CD4⁺ or CD8⁺, granulocytes as GRI^{hi}MAC1⁺ and monocytes as GRI^{lo}MAC1⁺. Foetal liver donor-derived cells (CD45.1⁺) were distinguished from residual recipient cells (CD45.1/2⁻). **g, h** Contribution of foetal liver (donor)-derived cells to peripheral blood populations at 4 weeks (**f**) and 20 weeks (**g**) post transplantation of the recipients described in (**e**). **i** Gating strategy for the assessment of stem and progenitor cells in the bone marrow of foetal liver transplant recipient mice. Cell types as indicated on the plots were distinguished by CD48 vs. CD150, CD34 vs. CD16.32 or IL7R α expression. (**j–k**) Contribution of foetal liver (donor)-derived cells to stem and progenitor populations in the bone marrow of foetal liver cell recipients at 20 weeks post-transplantation in CD48 vs. CD150 (**i**), CD34 vs. CD16/32 (**j**) cell populations. **l** Gating strategy for the assessment of B cell progenitors in the bone marrow of foetal liver transplant recipient mice. Cells were gated on single, viable cells co-expressing B220 and CD19 and distinguished by cKIT, IgM and IgD expression to identify the cell populations indicated in the plots. **m** Contribution of foetal liver (donor)-derived cells to bone marrow B cell progenitors 20 weeks post-transplant. Circles represent individual foetuses (**b**) or the mean of three recipients of a single foetal liver donor (**g, h, j, k, m**). Data are presented as mean \pm s.e.m. and were analysed using a one-way ANOVA (**b**) or two-way ANOVA with Tukey post hoc correction (**g, h, j, k, m**). HSCs, haematopoietic stem cells; LK; lineage marker negative cKIT⁻ cells; LSK, lineage marker negative SCA1⁺cKIT⁺ cells; HPC-1 (haematopoietic progenitor 1), HPC-2 (haematopoietic progenitor 2), MPP (multipotent progenitor), CLP (common lymphoid progenitor), CMP (common myeloid progenitor), GMP (granulocyte macrophage progenitors), MEP (megakaryocyte/erythroid progenitor). Granulo (granulocytes), Mono (monocytes); superscript: int, intermediate.

rescued in *Kat6a*^{-/-}*Tg(Kat6b)* embryos to the wild type position. Interestingly, the anterior boundary of *Hoxa5* expression in *Kat6a*^{+/+}*Tg(Kat6b)* embryos is not different to wild type littermate embryos. Similarly, *Hoxa3* expression, reduced and posteriorly shifted in *Kat6a*^{-/-}*Kat6b*^{+/+} embryos, is restored in *Kat6a*^{-/-}*Tg(Kat6b)* embryos to the wild type pattern of expression (Supplementary Fig. 7).

Kat6b overexpression rescued the cleft palate, cardiac and aortic arch defects observed in *Kat6a*^{-/-} mice

Kat6a^{-/-} mice have previously been shown to have cleft palate^{18,44}, ventricular septum defects^{18,45} and aortic arch defects¹⁸. Congruent with these previous studies, cleft palate (Fig. 5a, b), aortic arch defects (Fig. 5c, d) and ventricular septal defects (Fig. 5e) were observed in *Kat6a*^{-/-}*Kat6b*^{+/+} mice (Fig. 5a–e). Overexpression of *Kat6b* in *Kat6a*^{-/-}*Tg(Kat6b)* mice rescued each of these major phenotypic anomalies (Fig. 5a–e).

Kat6b overexpression rescued the pattern of H3K23 acetylation at *Kat6a* target loci

Western blot analysis showed that loss of KAT6A function results in a global reduction in H3K23ac in E9.5 embryos and MEFs, and that this is restored in the *Kat6a*^{-/-}*Tg(Kat6b)* condition. To examine specific genomic loci in more detail, in particular *Hox* clusters, *Tbx* and *Dlx* genes, we performed Cleavage Under Targets and Tagmentation (CUT&Tag) sequencing for H3K23ac. Since H3K23ac is one of the most abundant histone acetylation modifications and is widespread throughout the genome we used a *Drosophila* spike-in control to allow direct comparison between samples. Across samples H3K23ac showed a characteristic peak at the transcription start site (TSS) and a large difference between *Kat6a*^{-/-} vs. *Kat6b*^{+/+} in a multidimensional scaling plot (Supplementary Fig. 8a–c; Data 9). As expected, H3K23ac levels were reduced across the genome at 16889 loci in *Kat6a*^{-/-} samples compared to wild type controls (Fig. 6a; Supplementary Fig. 8d). This reduction in H3K23ac was completely reversed in cells prepared from *Kat6a*^{-/-}*Tg(Kat6b)* embryos (Fig. 6a; Supplementary Fig. 8e–g; Data 10–12). Specifically examining all *Hox* genes we found that H3K23ac was reduced in *Kat6a*^{-/-} cells compared to wild type and normal levels were restored in *Kat6a*^{-/-}*Tg(Kat6b)* cells (Fig. 6b).

Similarly at both *Tbx* and *Dlx* genes, H3K23ac was reduced in *Kat6a*^{-/-} cells and restored in *Kat6a*^{-/-}*Tg(Kat6b)* cells (Fig. 6c, d). Mapping individual reads across *Hox*, *Tbx* and *Dlx* loci (Fig. 6e–g) showed that H3K23ac was distributed across the gene body with distinctive peaks at promoters and other genomic features (Supplementary Fig. 8c). Unfortunately, we were unable to correlate the distribution of KAT6A or KAT6B with H3K23ac peaks as no CUT&Tag capable antibodies with the necessary specificity are available. The wild type pattern of peaks was faithfully reproduced in *Kat6a*^{-/-}*Tg(Kat6b)* cells (Fig. 6e–g).

Kat6b overexpression rescued the lethality of *Kat6a*^{-/-} mice

Overexpression of KAT6B rescued histone acetylation, gene expression patterns, transplantable HSCs, segment identity defects, heart and aortic arch defects and cleft palate previously described in *Kat6a*^{-/-}*Kat6b*^{+/+} mice. This demonstrates a complete rescue of all previously described developmental anomalies resulting from loss of KAT6A, including those that were incompatible with survival. To assess if perinatal lethality was rescued, *Kat6a*^{-/-}*Tg(Kat6b)* mice were allowed to develop to birth and were monitored in early life.

Kat6a^{-/-}*Kat6b*^{+/+} mice die between E14.5–E18.5 depending on the genetic background^{17,18}. Overexpression of *Kat6b* completely rescued this foetal to perinatal lethality. *Kat6a*^{-/-}*Tg(Kat6b)* mice developed normally in the postnatal period, even compared to *Kat6a* heterozygous (*Kat6a*^{+/-}) mice, which were notably runted in early life (Fig. 7a, b). Furthermore, *Kat6a*^{-/-}*Tg(Kat6b)* mice showed normal weight gain over the first 3 weeks of life, compared to reduced weight gain observed in both male and female *Kat6a*^{-/-} mice ($p = 0.001$ and 1×10^{-5} ; Fig. 7b). Remarkably, *Kat6a*^{-/-}*Tg(Kat6b)* mice of both sexes reached adulthood and were healthy and fertile. Among the offspring of *Kat6a*^{-/-}*Tg(Kat6b)* \times *Kat6a*^{+/+}*Kat6b*^{+/+} matings, *Kat6a*^{-/-}*Kat6b*^{+/+} mice were completely absent ($N = 0$ of 94; $p < 10^{-6}$; Fig. 7c). In contrast, *Kat6a*^{-/-}*Tg(Kat6b)* mice were present at the expected Mendelian ratio at weaning ($N = 32$ of 94; $p = 1$; Fig. 7c). This demonstrates that KAT6B overexpression in the absence of KAT6A not only rescued the effects of the homozygous loss of *Kat6a*, but improved development in early life compared to *Kat6a* heterozygosity.

Given the requirement for KAT6A in the adult haematopoietic system^{49,55}, bone marrow stem and progenitor populations were

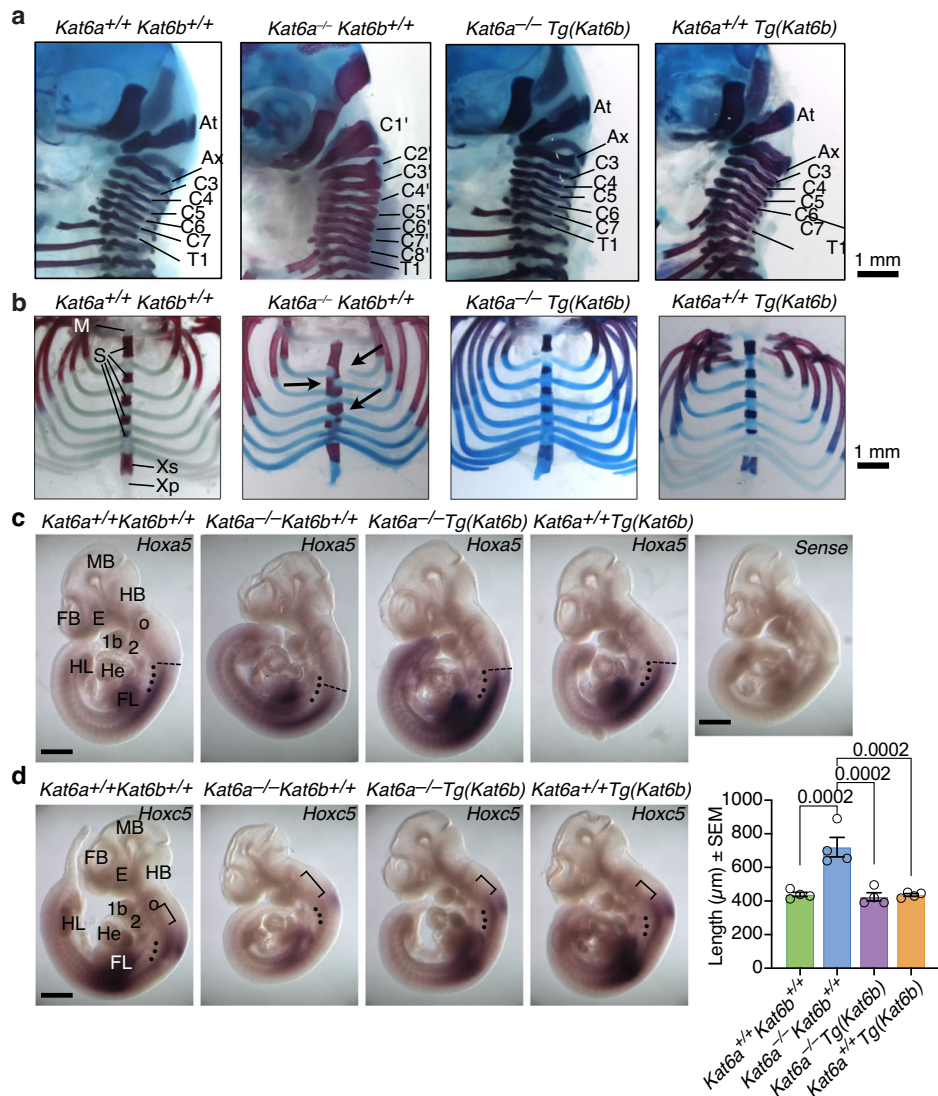


Fig. 4 | *Kat6b* overexpression rescues the anterior homeotic transformation seen in *Kat6a*^{-/-} mice. a, b Alizarin red (bone) and Alcian blue (cartilage) stained skeletal preparations of *N* = 9 *Kat6a*^{+/+}*Kat6b*^{+/+}, 1 *Kat6a*^{-/-}*Kat6b*^{+/+}, 4 *Kat6a*^{-/-}*Tg(Kat6b)* and 5 *Kat6a*^{+/+}*Tg(Kat6b)* E18.5 foetuses with labelled cervical vertebrae (a) and sternum (b), arrow indicates abnormal rib attachment (b). Note that embryos homozygous for this allele of *Kat6a* rarely survive until E18.5. Representative images are shown. Representative images of RNA/RNA whole-mount situ hybridisation to detect *Hoxa5* (c) and *Hoxc5* (d) mRNA in *Kat6a*^{+/+}*Kat6b*^{+/+}, *Kat6a*^{-/-}*Kat6b*^{+/+}, *Kat6a*^{-/-}*Tg(Kat6b)* and *Kat6a*^{+/+}*Tg(Kat6b)* E10.5 embryos, with anterior expression boundary indicated. Note no staining using the sense control probe (*n* = 3 wild type embryos). The 3–4 most cranial somites are indicated by a dot (c, d). The anterior expression boundary of *Hoxa5* is indicated by a stippled line (c). The distance between the anterior boundary of the *Hoxc5* expression domain in the neural tube and the caudal boundary of the otic vesicle is indicated by a bracket (d). The distance was measured and is displayed in the

bar graph in (d). *Hoxa5* *N* = 3, *Kat6a*^{+/+}*Kat6b*^{+/+}, *N* = 3, *Kat6a*^{-/-}*Kat6b*^{+/+}, *N* = 3, *Kat6a*^{-/-}*Tg(Kat6b)* and *N* = 3, *Kat6a*^{+/+}*Tg(Kat6b)* were used. *Hoxc5* *N* = 4, *Kat6a*^{+/+}*Kat6b*^{+/+}, *N* = 4, *Kat6a*^{-/-}*Kat6b*^{+/+}, *N* = 4, *Kat6a*^{-/-}*Tg(Kat6b)* and *N* = 4, *Kat6a*^{+/+}*Tg(Kat6b)* were used. This experiment was repeated a second time with each probe with *N* = 3 embryos per genotype. Data are presented as means ± s.e.m. and were analysed by one-way ANOVA with Tukey's multiple comparison test. Circles in the bar graph (d) represent individual embryos. 1b, mandibular region of the first pharyngeal arch; 2, second pharyngeal arch; At, atlas = 1st cervical vertebra, Cl; Ax, axis = 2nd cervical vertebra, C2; C1 to C7, 1st to 7th cervical vertebrae; C1' to C8', 1st to 8th abnormal *Kat6a*^{-/-}*Kat6b*^{+/+} cervical vertebrae, whereby C8' is supernumerary; E eye, FB forebrain, FL forelimb, HB hind-brain, He heart, HL hindlimb, M manubrium, MB midbrain, o otic vesicle, S sternbrae, T1 1st thoracic vertebra (rib bearing). Xp xiphoid process, Xs xiphisternum. Scale bar = 1 mm (a, b), 600 µm (c), 680 µm (d).

assessed in adult *Kat6a*^{-/-}*Tg(Kat6b)* mice at 12 weeks of age. All stem and progenitor populations showed similar frequencies as in wild-type control mice (Fig. 7d–h), indicating that haematopoietic development in adulthood is normal in *Kat6a*^{-/-}*Tg(Kat6b)* animals.

Discussion

In this study we demonstrate that KAT6B, expressed at 4-fold above endogenous levels in *Kat6a*^{-/-} mice, rescues the previously described developmental defects resulting from homozygous loss of KAT6A.

Remarkably, *Kat6a*^{-/-}*Tg(Kat6b)* mice are born, show normal development to adulthood and normal blood cell development in adulthood.

In addition to rescuing the anatomical defects resulting from loss of KAT6A, KAT6B overexpression reverted ~90% of the changes in gene expression caused by loss of KAT6A and re-established global acetylation levels at H3K9 and H3K23 in whole E9.5 embryos and H3K23 in MEFs. Examining locus-specific acetylation we found complete restoration of the normal pattern of H3K23ac down to the level of individual peaks within transcription units. The rescue of genes

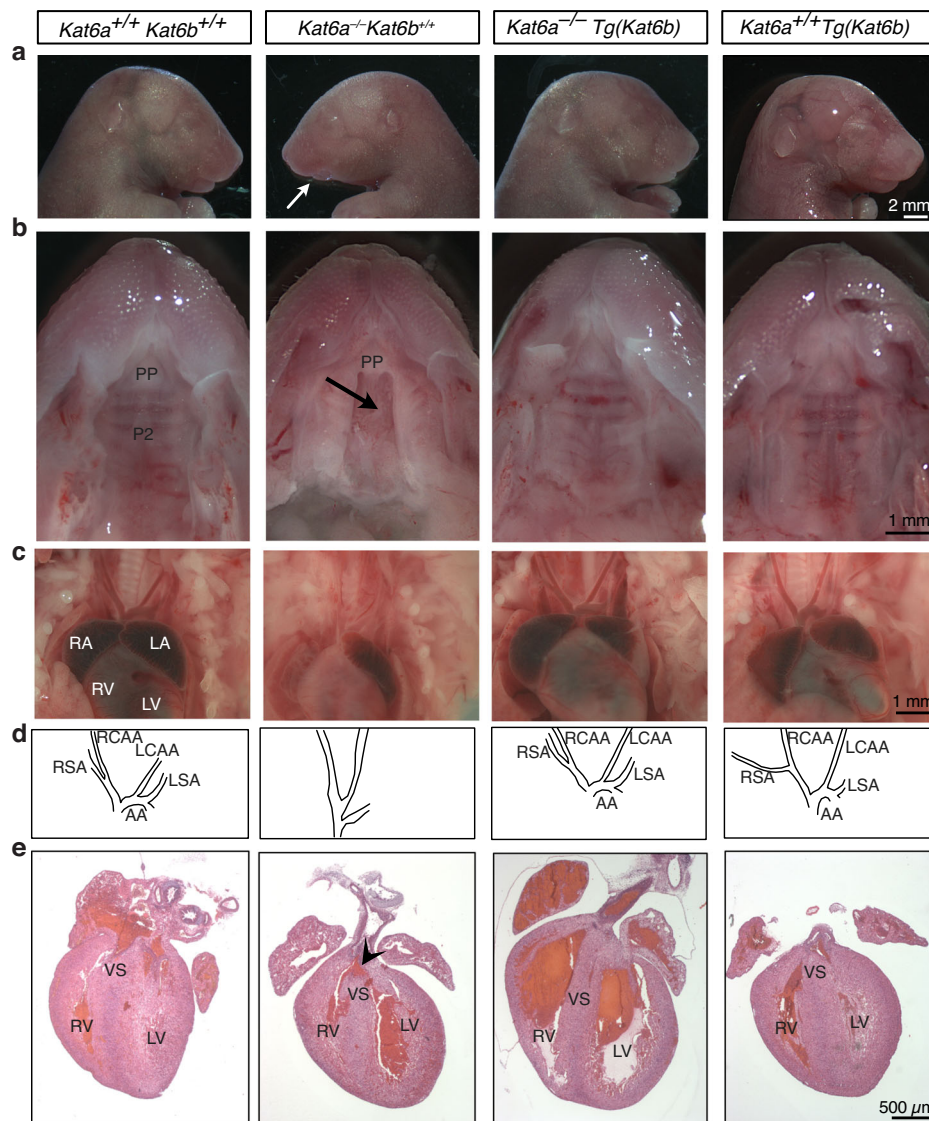


Fig. 5 | *Kat6b* overexpression rescues the cleft palate, aortic arch and cardiac defects observed in *Kat6a*^{-/-} mice. a–e Examination of *N* = 7 *Kat6a*^{+/+}*Kat6b*^{+/+}, *N* = 1 *Kat6a*^{-/-}*Kat6b*^{+/+}, *N* = 5 *Kat6a*^{-/-}*Tg(Kat6b)* and *N* = 6 *Kat6a*^{+/+}*Tg(Kat6b)* fetuses at E18.5 during dissection and by histopathology. Note that embryos homozygous for this allele of *KAT6a* rarely survive until E18.5. **a** Lateral view of the head and neck of E18.5 *Kat6a*^{+/+}*Kat6b*^{+/+}, *Kat6a*^{-/-}*Kat6b*^{+/+}, *Kat6a*^{-/-}*Tg(Kat6b)* and *Kat6a*^{+/+}*Tg(Kat6b)* fetuses. The arrow indicates an underdeveloped lower jaw in the *Kat6a*^{-/-}*Kat6b*^{+/+} mouse. **b** Ventral view of the palate of E18.5 *Kat6a*^{+/+}*Kat6b*^{+/+}, *Kat6a*^{-/-}*Kat6b*^{+/+}, *Kat6a*^{-/-}*Tg(Kat6b)* and *Kat6a*^{+/+}*Tg(Kat6b)* fetuses. The arrow indicates a cleft palate

in the *Kat6a*^{-/-}*Kat6b*^{+/+} mouse. **c, d** Images of the heart and aortic arch of *Kat6a*^{+/+}*Kat6b*^{+/+}, *Kat6a*^{-/-}*Kat6b*^{+/+}, *Kat6a*^{-/-}*Tg(Kat6b)* and *Kat6a*^{+/+}*Tg(Kat6b)* E18.5 fetuses (**c**). Traces of the aortic arch and arteries (**d**). **e** H&E sections of the hearts of *Kat6a*^{+/+}*Kat6b*^{+/+}, *Kat6a*^{-/-}*Kat6b*^{+/+}, *Kat6a*^{-/-}*Tg(Kat6b)* and *Kat6a*^{+/+}*Tg(Kat6b)* E18.5 fetuses. Arrowhead indicates the ventricular septal defect in *Kat6a*^{-/-}*Kat6b*^{+/+} animals. AA aortic arch, LA left atrium, LCAA left common carotid artery, LSA left subclavian artery, LV left ventricle, P2 secondary palate, PP primary palate, RA right atrium, RCAA right common carotid artery, RSA right subclavian artery, RV right ventricle, VS ventricular septum. Scale bars are 2 mm (**a**), 1 mm (**b, c**), 500 μm (**e**).

downregulated in *Kat6a*^{-/-}*Kat6b*^{+/+} mice by *KAT6B* overexpression is particularly interesting, as *KAT6B* is not ordinarily required for expression of many *KAT6A*-dependent genes. In particular, while *KAT6A* is essential for the normal expression the *Hox*, gene families, *KAT6B* has no role in regulation of these genes and the axial skeleton develops normally without *KAT6B*. The capacity of overexpressed *KAT6B* to carry out the role of promoting their expression in the absence of *KAT6A* indicates that any target gene specificity of *KAT6A* arising from the differences in amino acid sequence between *KAT6A* and *KAT6B*, and perhaps affecting protein-protein interaction, can be overcome by higher levels of *KAT6B*.

In utero treatment with retinoic acid, an activator of *Hox* gene expression^{56,57}, rescues the anterior homeotic transformation in *Kat6a*^{-/-} mice, but not other developmental defects¹⁷. Indeed, *in utero* retinoic acid treatment causes cardiac defects in *Kat6a*^{+/+} mice¹⁸.

Conversely, the cardiac septum defect of *Kat6a*^{-/-} mice was rescued by overexpressing the *Tbx1* gene¹⁸. Body segment identity has been restored in *Kat6a*^{-/-} mice by additionally deleting *Bmi1*⁵⁴. *BMI1* is a polycomb repressor protein that represses *Hox* gene expression and, when deleted, causes a posterior homeotic transformation^{58,59}. Combined deletion of *Kat6a* and *Bmi1* genes was found to restore the respective anterior and posterior homeotic transformations observed in single mutant mice⁵⁴, but did not rescue the haematopoietic defects of *Kat6a*^{-/-} mice⁵⁵. Collectively, these results suggest that *KAT6A* does not act as a binary on-off switch, but rather the level of *KAT6A* activity acts to balance the activity of repressors to generate an appropriate level of gene expression in a cell-type specific context.

Our data suggest that *KAT6B* overexpression in the absence of *KAT6A* may result in a more favourable stoichiometry of complex

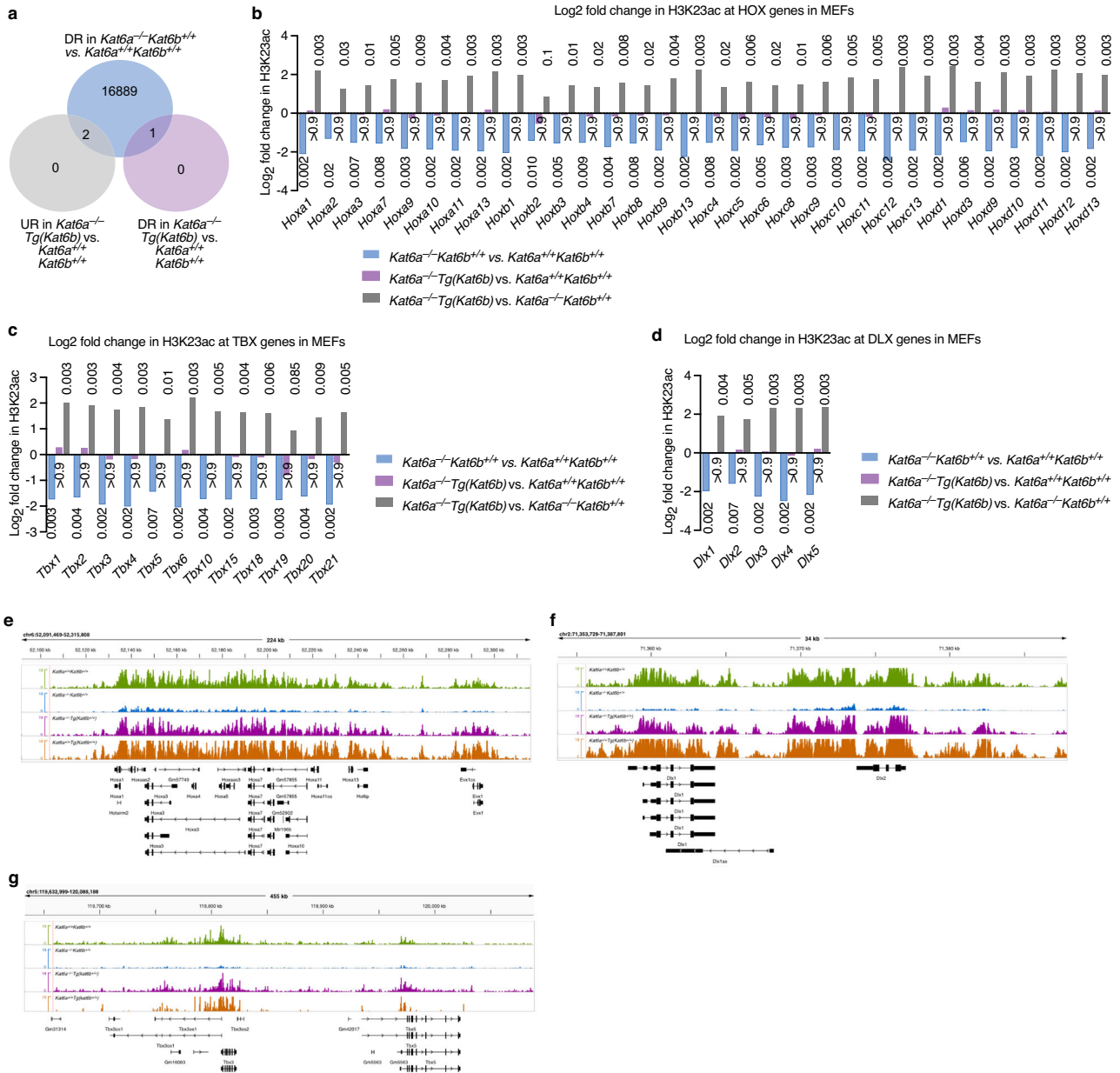


Fig. 6 | Decrease in H3K23ac in *Kat6a*^{-/-} cells restored to normal in *Kat6a*^{-/-}*Tg(Kat6b)* cells. **a–g** CUT&Tag results detecting histone H3 lysine 23 acetylation (in H3K23ac) in primary mouse embryonic fibroblasts isolated from E14.5 *Kat6a*^{+/-}*Kat6b*^{+/-}, *Kat6a*^{-/-}*Kat6b*^{+/-}, *Kat6a*^{-/-}*Tg(Kat6b)* and *Kat6a*^{-/-}*Tg(Kat6b)* E10.5 foetuses. *N* = 4 foetuses per genotype. Data were analysed as described in the ‘methods’ section. A false discovery rate (FDR) of less than 0.05 was considered significant. **a** Venn diagram showing number of genes with reduced H3K23ac levels in the indicated samples compared to wild type controls. In comparison to wild

type cells *Kat6a*^{-/-} cells show a global reduction in H3K23ac which is restored to normal in *Kat6a*^{-/-}*Tg(Kat6b)* cells. **b–d** Log₂ fold changes in H3K23ac levels at HOX genes (**b**), TBX genes (**c**) and DLX genes (**d**). Note that the reduction in H3K23ac in *Kat6a*^{-/-} MEFs is restored to normal in *Kat6a*^{-/-}*Tg(Kat6b)* MEFs. The FDR is indicated above or below each bar. **e–g** Read depth plots of H3K23ac in the HOXA gene cluster (**e**), at the *Dlx1/Dlx2* locus (**f**) and at the *Tbx3/Tbx5* locus. Note that the characteristic distribution of H3K23ac in wild type cells is restored in *Kat6a*^{-/-}*Tg(Kat6b)* cells.

subunits to allow KAT6B to take on the role of KAT6A, compared to endogenous levels of KAT6B or KAT6B overexpression in the presence of KAT6A. In the absence of KAT6A, the limitation of auxiliary complex member availability may permit KAT6B, when overexpressed, to perform its own typical roles, as well as those of KAT6A, without spurious effects resulting from an overabundance of KAT6B. This is evident at the level of global histone acetylation, as acetylation levels at H3K9 and H3K23 in *Kat6a*^{-/-}*Tg(Kat6b)* E9.5 embryos were similar to wild type controls, while these residues were hyperacetylated in *Kat6a*^{+/-}*Tg(Kat6b)* samples.

Notwithstanding the profound rescue of the expression levels of genes downregulated in *Kat6a*^{-/-}*Kat6b*^{+/-} embryos at E9.5 when *Kat6b*

is overexpressed, some effects of the loss of KAT6A persisted. When only *Tbx* genes were considered (as opposed to transcriptome-wide analyses), *Tbx1* and *15* were still significantly downregulated in *Kat6a*^{-/-}*Tg(Kat6b)* embryos compared to wild type control embryos. However, *Tbx1* was significantly increased in *Kat6a*^{-/-}*Tg(Kat6b)* embryos compared to *Kat6a*^{-/-}*Kat6b*^{+/-} samples. This partial rescue was sufficient to rescue the cardiac defects of *Kat6a*^{-/-}*Kat6b*^{+/-} mice, consistent with the rescue of heart defects in *Kat6a*^{-/-} mice by transgenic overexpression of *Tbx1*¹⁸.

In addition to rescuing congenital defects resulting from loss of KAT6A, KAT6B overexpression restored the formation of definitive HSCs capable of reconstituting the haematopoietic system of

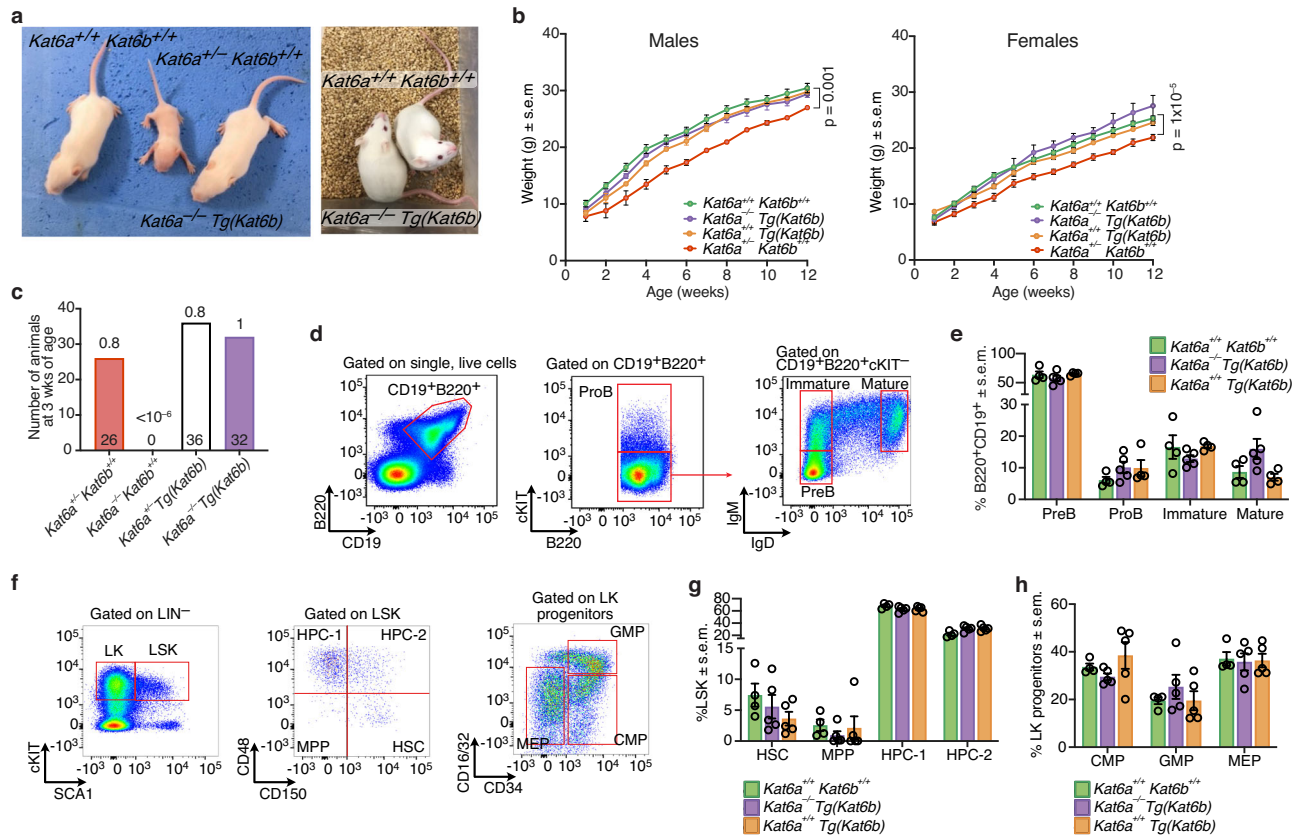


Fig. 7 | *Kat6b* overexpression rescues the perinatal lethality of *Kat6a*^{-/-} mice. **a** Representative photographs of wild type, *Kat6a*^{-/-}*Kat6b*^{+/+} and *Kat6a*^{-/-}*Tg(Kat6b)* mice at postnatal day 7 (left) and *Kat6a*^{+/+}*Kat6b*^{+/+} and *Kat6a*^{-/-}*Tg(Kat6b)* mice at 12 weeks of age (right). **b** Weights of *Kat6a*^{+/+}*Kat6b*^{+/+} (23 female; 16 male), *Kat6a*^{-/-}*Kat6b*^{+/+} (16 female; 4 male), *Kat6a*^{-/-}*Tg(Kat6b)* (4 female; 4 male) and *Kat6a*^{-/-}*Tg(Kat6b)* (4 female; 4 male) mice from postnatal week 1 to week 12. Data presented as mean \pm s.e.m. and were analysed using a two-way ANOVA with Holm-Sidak post-hoc correction. **c** Genotypes at 3 weeks of age of offspring ($N = 94$) of matings with the parental genotypes *Kat6a*^{-/-}*Kat6b*^{+/+} \times *Kat6a*^{-/-}*Tg(Kat6b)*. The observed genotype frequency was compared to the expected Mendelian frequencies, p values of the binomial probability testing if a genotype was observed

differed from the expected frequency are shown (two sided). **d-h** Flow cytometry analysis of the bone marrow of $N = 4$ adult *Kat6a*^{+/+}*Kat6b*^{+/+}, 5 *Kat6a*^{-/-}*Tg(Kat6b)* and 5 *Kat6a*^{+/+}*Tg(Kat6b)* mice. Flow cytometry gating strategies defining haematopoietic cell population using cell surface markers as described in Fig. 4. Each circle represents an individual mouse. Data in (e, g, h) are presented as mean \pm s.e.m. Each circle represents an individual mouse. Data were analysed using a two-way ANOVA with Tukey post-hoc correction. Abbreviations as defined in Fig. 4. Flow cytometry gating strategy (d) and analysis (e) of B cell progenitor populations in the bone marrow. Gating strategy (f) and analysis (g, h) of haematopoietic stem and progenitor population in the bone marrow.

irradiated recipient mice. Paralleling a previous report that loss of KAT6A reduces CD8 cell surface expression⁶⁰, we found that KAT6B overexpression promoted CD8 T cell formation at the expense of CD4 T cell development in transplant recipient mice, and that this effect of overexpressed KAT6B was modulated by the loss of KAT6A.

Recently, inhibitors have been developed for both CBP/p300⁶¹ and KAT6A/KAT6B³⁰ protein pairs with the view of developing novel cancer therapeutics. Currently, the KAT6A/KAT6B inhibitors are in clinical trials for the treatment of solid cancers^{31,32,62}. In the process of developing these inhibitors it has become clear that it would be unlikely that any inhibitor would differentially inhibit one and not the other of each of these protein pairs. It is therefore relevant to determine the functional equivalence of the proteins within pairs. The combined deletion of these proteins only reveals how similar their functions are at endogenous expression levels. In contrast, our data on the rescue of the *Kat6a*^{-/-} mice by overexpression of KAT6B indicate that KAT6B can replace KAT6A so completely that it can rescue the 100% lethality, producing healthy and fertile mice that lack KAT6A. These results suggest that simultaneous inhibition of both KAT6A and KAT6B function is likely to be beneficial in treating cancers dependent on KAT6 activity.

Methods

Mice

All animal experiments were conducted with approval of the WEHI Animal Ethics Committee and according to the Australian code for the care and use of animals for scientific purposes. Mice were kept in a 14 h light/10 h dark cycle. Noon of the day the vaginal copulation plug was first observed was defined as embryonic day 0.5 (E0.5).

Mouse alleles

The *Kat6a* null allele used in this study lacked exons 5 to 9 and has been described previously¹⁷. KAT6B overexpression transgenic mice were generated by microinjected into mouse pronuclei using bacterial artificial chromosome (BAC) *pBACe3.6* clone *RP23-360F23* to produce a germline founder. BAC clone *RP23-360F23* includes the complete wild-type *Kat6b* gene, as well as 21 kb 5' and 42 kb 3' containing regulatory sequences. Seven copies of the BAC inserted into the mouse genome to result in an \sim 4-fold increase in *Kat6b* expression as described previously²³. Mice were maintained on a *FVB* \times *BALB/c* hybrid background as *Kat6b* overexpressing mice were not viable on inbred backgrounds. Mice were genotyped by genomic 3-way PCR for the *Kat6a* allele and by simple PCR to detect the *SacB* gene in the backbone of *pBACe3.6* clone *RP23-360F23* using the primers listed in Supplementary Table 1.

Primary mouse embryonic fibroblast (MEF)

MEFs were derived from E14.5 fetuses and grown in Dulbecco's modified Eagle medium (Gibco, 11995) supplemented with 100 U/ml penicillin/streptomycin (Gibco, 15140122) and 10% foetal calf serum. Cells were cultured in at 37 °C, 5% CO₂ and 3% O₂. Cell counts were determined at each passage using a Countess™ cell counter (ThermoFisher).

Acid histone extraction

MEFs were washed in DPBS (Gibco, 14190144) containing 0.5 mM sodium butyrate (Sigma, B5887) and cOmplete™ EDTA-free protease inhibitor cocktail (Roche, 11873580001), scraped using a cell scraper (Fisher Scientific, 08-100-241) and collected by centrifugation (200 × g, 5 min). Whole E9.5 embryos were dissected and photographed under a dissecting microscope (Zeiss) and placed into a 1.5 ml Eppendorf tube containing 100 µl DPBS with 0.5 mM sodium butyrate (Sigma, B5887) and cOmplete™ EDTA-free protease inhibitor cocktail (Roche, 11873580001). Samples were lysed in Histone acid lysis buffer (10 mM HEPES pH 7.9, 1.5 mM MgCl₂, 10 mM KCl and 0.5 mM DTT) for 30 min at 4 °C on a roller, collected by centrifugation (10,000 × g, 10 min) and resuspended in 0.2 M H₂SO₄. Samples were incubated on ice for 1–2 h before being dialysed in dialysis tubing (Spectrum™ Spectra/Por Dialysis Membrane Tubing; molecular weight cut-off 20 kDa; Fisher Scientific, 08-607-067) against 0.1 M acetic acid (Sigma, A6283) for 1 h at 4 °C and MQ-H₂O overnight at 4 °C. Protein concentrations were determined using a bicinchoninic acid (BCA) assay (ThermoFisher, 23225).

Western immunoblotting

Acid extracted histones were run on 4–12% Bis-Tris gels (ThermoFisher, NP0322) and transferred onto nitrocellulose membranes (Licor, 926-31090). Membranes were blocked for 1 h at room temperature (RT) on a roller in blocking buffer (Intercept® (PBS); Licor, 927-70001) and probed with antibodies against H3K9ac (Epicypheer, 13-0033; dilution 1:5000), H3K14ac (Abcam, ab52946; 1:1000) or H3K23ac (Millipore, 07-355; 1:5000) and pan H3 (Abcam, 10799; 1:5000) overnight at 4 °C. The following morning membranes were washed in PBS + 0.1% Tween-20 (Sigma, P1379) and incubated with goat anti-mouse IgG secondary (IRDye® 800 CW; LI-COR Biosciences 926-32210; 1:10,000) and goat anti-rabbit IgG (IRDye®; LI-COR Biosciences, 926-68071; 1:10,000) secondary antibodies for 1 h at RT on a roller. Samples were imaged and analysed using an automated western blot imager software (Odyssey Imager; LI-COR Biosciences).

Histology

E18.5 hearts were dissected, washed in PBS and fixed overnight in 10% neutral buffered formalin. Hearts were embedded in agarose to control orientation, then dehydrated and infused with paraffin and embedded for histological sectioning and haematoxylin and eosin (H&E) staining.

Skeletal preparations

Skin and internal organs were removed from E18.5 pups under a dissecting microscope (Zeiss). Pups were fixed in 4% PFA (Sigma, 158127) overnight at RT on a roller, briefly rinsed in 95% EtOH and stained overnight at RT in a solution containing 5 ml 0.4% Alcian Blue 8 GX (w/v), 5 ml glacial acetic acid, 70 ml 95% EtOH, 20 ml MQ-H₂O and 100 µl 0.5% Alizarin red (w/v). Samples were washed in MQ-H₂O. Soft tissues were dissolved in 2% (w/v) KOH (Sigma, 221473) in H₂O for 24 h at RT on a roller. Following digestion, skeletal preparations were washed in 0.25% (w/v) KOH in H₂O for 30 min at RT on a roller, followed by ascending concentrations of glycerol (20%, 33%, 50%) in 0.25% (w/v) KOH in H₂O, for 1 h, 1 h and overnight, respectively at RT on a roller. Prepared skeletons were stored in 50% (w/v) glycerol (Sigma, G5516) in ddH₂O.

Whole mount in situ hybridization

Embryos used for whole-mount in situ hybridisation were fixed in 4% paraformaldehyde overnight then dehydrated through a methanol series and stored at –20 °C. After genotyping selected embryos were rehydrated through a methanol series, washed in phosphate buffer saline/Tween20, then bleached in hydrogen peroxide, washed in phosphate buffer saline/Tween20, then treated with proteinase K which was stopped by the addition of 1 M glycine. Embryos were then prehybridised a solution of 50% Formamide/5x SSC pH4.5/ 1% SDS/ 50 µg/ml yeast RNA/ 50 µg/ml heparin for 1 h. Embryos were then transferred to a fresh aliquot of the hybridisation buffer containing in vitro transcribed (Roche 11175025910), digoxigenin-labelled cRNA of the *Hox* gene under investigation and incubated at 55 °C overnight. Then embryos were washed extensively, treated with RnaseA, blocking reagent (Roche 10057177103) and foetal bovine serum, incubated with alkaline phosphatase- labelled anti-digoxigenin antibody (Roche 11214667001) overnight, washed extensively, followed by alkaline phosphatase reaction with NBT-BCIP (Roche 11681451001) for colour development. Finally, embryos were washed and then cleared in glycerol⁶³. Sense and antisense probes for *Hoxa3*, *Hoxa5* and *Hoxc5* have been previously described^{17,54}.

Foetal liver transplantation

E14.5 foetal livers were dissected and passed through a 40 µm cell sieve (Corning, 431750). 1 × 10⁶ cells, as determined using an automated haematology analyser (Advia 2120i, Siemens Healthineers), were injected into the tail vein of 3x irradiated recipients (2 × 550 rad, 3 h apart)⁴⁹.

Flow cytometry

Erythrocytes were lysed by washing samples 2 × 10 ml in a hypotonic solution (150 mM NH₄Cl, 0.1 mM EDTA, 12 mM NaHCO₃, pH 7.2). Cells were resuspended in a FACS buffer (150 mM NaCl, 3.7 mM KCl, 2.5 mM CaCl₂·2H₂O, 1.2 mM MgSO₄·7H₂O, 0.8 mM K₂HPO₄, 1.2 mM KH₂PO₄, 11.5 mM HEPES, pH 7.4) supplemented with 2% foetal calf serum and stained with conjugated antibodies (Supplementary Table 2) for 1 h on ice. Samples were washed in 3–4 ml FACS buffer and analysed on a flow cytometer (BD LSRFortessa™ X-20, BD) at <7500 events/sec. Data were analysed using flow cytometry analysis software (FlowJo version 10.7, Tree Star Inc.). Cell surface markers used to identify individual cell types are shown in Supplementary Table 3.

RNA isolation and sequencing

Total RNA from whole E9.5 embryos was extracted using an RNA extraction kit (Qiagen RNeasy mini kit; Qiagen, 74104), according to the manufacturer's instructions and including the optional DNaseI digestion step. RNA quality and quantity were assessed on an automated analyser (Tapestation 4200; Agilent, G2991BA), and 500 ng RNA used to generate libraries using a library construction kit (TruSeq RNA prep kit v2; Illumina, RS-122-2002), according to the manufacturer's instructions. Samples were run on a sequencing machine (NextSeq 2000; Illumina) to give 66 bp paired end reads.

RNA sequencing analysis

Reads were aligned to the *Mus musculus* (mm39) genome using Rsubread⁶⁴. Differential expression (DE) analyses were performed using the edgeR and limma software packages⁶⁵. Library sizes were normalised using the trimmed mean of *M*-values (TMM) method⁶⁶ and the surrogate variable approach⁶⁷ was used to adjust for unwanted variation in the data. The false discovery rate (FDR) was controlled below 0.05. R version 4.2.2 was used for all analyses.

Cut&Tag detection of H3K23 acetylation

CUT&Tag sequencing was performed on 50,000 MEFs combined with 50,000 *Drosophila melanogaster* S2 cells, as described in Kaya-Okur et al.⁶⁸, with minor modifications as described in ref. 69. All buffers

were prepared fresh with complete EDTA-free protease inhibitors (Roche, 11873580001) and 0.5 mM sodium butyrate (Sigma, B5887). Per sample, 10 μ l concanavalin-A beads (Bangs Laboratories, BP531) were washed twice in 10 volumes binding buffer (20 mM HEPES pH 7.5 (Sigma, 83264), 10 mM KCl (Sigma, 60142), 1 mM CaCl₂ (Sigma, 21115) and 1 mM MnCl₂ (Sigma, M1787) and resuspended in 10 μ l binding buffer. Combined MEFs and S2 *D. melanogaster* cells were washed twice in 1 ml wash buffer (20 mM HEPES pH 7.5, 150 mM NaCl (Sigma, 71386), 0.5 mM spermidine (Sigma, SO266) and resuspended in 90 μ l wash buffer. Concanavalin-A beads and samples were combined and incubated (RT, 10 min), immobilised using a magnetic rack (ThermoFisher, MR02) and beads resuspended in 100 μ l ice-cold antibody buffer (wash buffer supplemented with 0.05 % (w/v) digitonin (Merck, 300410), 2 mM EDTA (Invitrogen, 15575020) and 0.1 % (w/v) BSA (Sigma, A8577) containing 1:100 H3K23ac (Millipore, 07-355) primary antibody. Samples were incubated overnight at 4 °C. The following morning, beads were resuspended in 100 μ l wash buffer supplemented with 0.05 % (w/v) digitonin containing 1:100 secondary antibody (Guinea pig anti-rabbit IgG, Antibodies Online, ABIN101961), incubated (RT, 1 h), washed thrice and resuspended in 100 μ l ice-cold dig-300 buffer (20 mM HEPES pH 7.5, 300 mM NaCl, 0.5 mM spermidine and 0.01 % (w/v) digitonin), supplemented with 1 2.5 μ l pAG-Tn5 (EpiCypher, 15-1017). Samples were incubated (RT, 1 h), washed thrice, resuspended in 100 μ l tagmentation buffer (wash buffer supplemented with 0.01 mM MgCl₂ (Sigma, 63069) and incubated at 37 °C for 1 h. Tagmentation was stopped using 3.34 μ l 0.5 M EDTA, 1 μ l 10 % (w/v) SDS (Sigma, 71736), and 0.83 μ l 20 mg/ml thermolabile proteinase K (NEB, P8111S), incubating at 37 °C for 1 h and 800 rpm, followed by heat inactivation at 55 °C for 10 min. DNA was extracted using Ampure XP beads (Beckman, A63880), eluting in 25 μ l 10 mM Tris-HCl pH = 8.0 (Invitrogen, 15568025), 1 mM EDTA and 25 μ g/ml RNase A (ThermoFisher, EN0531) at 37 °C for 10 min. 10 μ l sample DNA elutes were used to generate sequencing libraries, which were amplified using PCR for 13 cycles. PCR products were cleaned up using 30 μ l Ampure XP beads and eluted in 25 μ l 10 mM Tris-HCl pH 8.0. Cleaned libraries were analysed using High Sensitivity D1000 gels (Agilent, 5067-5584) on an Agilent 2200 tape station. Libraries were sequenced using an Illumina NextSeq2000.

Analysis of CUT&Tag data

All samples were composed of *Mus musculus* (test) and *Drosophila melanogaster* RNA (spike-in for normalisation⁷⁰). Furthermore, the transgenic BAC backbone samples contained the *sacB* gene. For alignment an index was built using Rsubread v2.18.0⁷¹ containing the mouse genome (mm39), the *Drosophila* genome (R655) and the *sacB* gene sequence. All samples were aligned to this combined genome index using Rsubread's align function reporting uniquely mapped reads only. All PCR duplicate reads were then marked using sambamba v0.6.6. The data was then summarised at both the species and mouse gene level. Data around mouse genes was summarised at -1 kbp upstream of the TSS to the TSS, transcription end site (TES) to +1kbp downstream of the TES, and the gene body (TSS to TES). Fragment counts were produced using Rsubread's featureCounts function. Fragments were counted if they were not a PCR duplicate and non-chimeric. Mouse genes were identified using RefSeq annotation to the mm39 genome. The analysis of each region was restricted to protein coding genes with official gene symbols. Riken, Gm (predicted), and pseudogenes were also removed. To avoid sex-based biases, the Xist gene and Y-chromosome were removed. Analysis of each region was then conducted independently. Differential analyses were conducted using the limma⁶⁵ and edgeR⁶⁶ software packages, versions 3.60.4 and 4.2.1 respectively.

For each analysis, lowly abundant regions were filtered using edgeR's filterByExpr function with default parameters. The samples were then normalised to *Drosophila melanogaster* content using the following method:

1. Calculate total *drosophila* content for each sample.
2. Divide the above by the total filtered mouse counts for that sample.
3. Divide the resulting numbers by the product of all values calculated in step 2 to the power of (1/number of samples).

Differential analyses between genotypes were then conducted as follows.

TSS region: the data was transformed to log₂-counts per million (CPM) and sample weights were calculated using limma's arrayWeights function using the genebygene method⁷². Linear models were fit to each region and robust empirical bayes moderated t-statistics with a trended prior variance were then applied to identify differential regions (robust limma-trend pipeline with sample weights)⁷³.

Gene body region: the data was transformed to log₂CPM with associated precision weights using voom. Linear models were then fit to each genomic region, differences between groups were assessed using robust empirical bayes moderated t-statistics (robust limma-voom pipeline)⁷³.

TES region: Limma's voomWithQualityWeights function was applied to simultaneously transform the data to log₂CPM with associated precision weights and estimate sample level weights⁷⁴. Linear models were then fit to each genomic region, differences between groups were assessed using robust empirical bayes moderated t-statistics (robust limma-voomWithQualityWeights pipeline).

For each analysis the false discovery rate (FDR) was controlled below 5% using the Benjamini and Hochberg method.

Statistics

The statistical analysis methods for the RNA-sequencing and CUT&Tag data are provided under the *RNA-sequencing analysis* and *Analysis of CUT&Tag data* section. Other data are presented as mean \pm s.e.m. In all graphs circles represent individual mice or the average of transplant recipients that received cells from a single foetal liver donor. Statistical analyses were performed in Prism Graphpad Version 8.3.1 for Mac (GraphPad Software) and R version 4.2.2. Statistical tests employed and the number of biological replicates are stated in the figure legends.

Reporting summary

Further information on research design is available in the Nature Portfolio Reporting Summary linked to this article.

Data availability

All RNA sequencing and CUT&Tag data has been deposited in the NCBI GEO database under accession numbers: [GSE287243](https://www.ncbi.nlm.nih.gov/geo/query/acc.cgi?acc=GSE287243) and [GSE287244](https://www.ncbi.nlm.nih.gov/geo/query/acc.cgi?acc=GSE287244) [<https://www.ncbi.nlm.nih.gov/geo/query/acc.cgi?acc=GSE287244>]. Source data are provided with this paper.

References

1. Strahl, B. D. & Allis, C. D. The language of covalent histone modifications. *Nature* **403**, 41–45 (2000).
2. Wang, Z. et al. Combinatorial patterns of histone acetylations and methylations in the human genome. *Nat. Genet.* **40**, 897–903 (2008).
3. Wang, Z. et al. Genome-wide mapping of HATs and HDACs reveals distinct functions in active and inactive genes. *Cell* **138**, 1019–1031 (2009).
4. Sheikh, B. N. & Akhtar, A. The many lives of KATs—detectors, integrators and modulators of the cellular environment. *Nat. Rev. Genet.* **20**, 7–23 (2019).
5. Voss, A. K. & Thomas, T. Histone lysine and genomic targets of histone acetyltransferases in mammals. *Bioessays* **40**, e1800078 (2018).
6. Thomas, T. & Voss, A. K. The diverse biological roles of MYST histone acetyltransferase family proteins. *Cell Cycle* **6**, 696–704 (2007).

7. Neuwald, A. F. Landsman D. GCN5-related histone N-acetyltransferases belong to a diverse superfamily that includes the yeast SPT10 protein. *Trends Biochem. Sci.* **22**, 154–155 (1997).
8. Arany, Z., Sellers, W. R., Livingston, D. M. & Eckner, R. E1A-associated p300 and CREB-associated CBP belong to a conserved family of coactivators. *Cell* **77**, 799–800 (1994).
9. Xu, W., Edmondson, D. G. & Roth, S. Y. Mammalian GCN5 and P/CAF acetyltransferases have homologous amino-terminal domains important for recognition of nucleosomal substrates. *Mol. Cell Biol.* **18**, 5659–5669 (1998).
10. Arany, Z., Newsome, D., Oldread, E., Livingston, D. M. & Eckner, R. A family of transcriptional adaptor proteins targeted by the E1A oncoprotein. *Nature* **374**, 81–84 (1995).
11. Lundblad, J. R., Kwok, R. P., Lurance, M. E., Harter, M. L. & Goodman, R. H. Adenoviral E1A-associated protein p300 as a functional homologue of the transcriptional co-activator CBP. *Nature* **374**, 85–88 (1995).
12. Soskine, M. & Tawfik, D. S. Mutational effects and the evolution of new protein functions. *Nat. Rev. Genet.* **11**, 572–582 (2010).
13. Kasper, L. H., Lerach, S., Wang, J., Wu, S., Jeevan, T. & Brindle, P. K. CBP/p300 double null cells reveal effect of coactivator level and diversity on CREB transactivation. *EMBO J.* **29**, 3660–3672 (2010).
14. Yamauchi, T. et al. Distinct but overlapping roles of histone acetylase PCAF and of the closely related PCAF-B/GCN5 in mouse embryogenesis. *Proc. Natl. Acad. Sci. USA* **97**, 11303–11306 (2000).
15. Doyon, Y. et al. ING tumor suppressor proteins are critical regulators of chromatin acetylation required for genome expression and perpetuation. *Mol. Cell* **21**, 51–64 (2006).
16. Ullah, M. et al. Molecular architecture of quartet MOZ/MORF histone acetyltransferase complexes. *Mol. Cell Biol.* **28**, 6828–6843 (2008).
17. Voss, A. K., Collin, C., Dixon, M. P. & Thomas, T. Moz and retinoic acid coordinately regulate H3K9 acetylation, Hox gene expression, and segment identity. *Dev. Cell* **17**, 674–686 (2009).
18. Voss, A. K. et al. MOZ regulates the Tbx1 locus, and Moz mutation partially phenocopies DiGeorge syndrome. *Dev. Cell* **23**, 652–663 (2012).
19. Simo-Riudalbas, L. et al. KAT6B is a tumor suppressor Histone H3 Lysine 23 acetyltransferase undergoing genomic loss in small cell lung cancer. *Cancer Res.* **75**, 3936–3945 (2015).
20. Klein, B. J. et al. Histone H3K23-specific acetylation by MORF is coupled to H3K14 acylation. *Nat. Commun.* **10**, 4724 (2019).
21. Lv, D. et al. Histone acetyltransferase KAT6A upregulates PI3K/AKT signaling through TRIM24 binding. *Cancer Res.* **77**, 6190–6201 (2017).
22. Bergamasco, M. I. et al. KAT6B is required for histone 3 lysine 9 acetylation and SOX gene expression in the developing brain. *Life Sci. Alliance* **8**, e202402969 (2025).
23. Bergamasco, M. I. et al. The histone acetyltransferase KAT6B is required for hematopoietic stem cell development and function. *Stem Cell Rep.* **19**, 469–485 (2024).
24. Borrow, J. et al. The translocation t(8;16)(p11;p13) of acute myeloid leukaemia fuses a putative acetyltransferase to the CREB-binding protein. *Nat. Genet.* **14**, 33–41 (1996).
25. Viita, T. & Cote, J. The MOZ-BRPF1 acetyltransferase complex in epigenetic crosstalk linked to gene regulation, development, and human diseases. *Front. Cell Dev. Biol.* **10**, 1115903 (2022).
26. Sheikh, B. N. et al. MOZ regulates B-cell progenitors and, consequently, Moz haploinsufficiency dramatically retards MYC-induced lymphoma development. *Blood* **125**, 1910–1921 (2015).
27. Trecourt, A. et al. The KAT6B::KANS1 fusion defines a new uterine sarcoma with hybrid endometrial stromal tumor and smooth muscle tumor features. *Mod. Pathol.* **36**, 100243 (2023).
28. Murati, A. et al. Variant MYST4-CBP gene fusion in a t(10;16) acute myeloid leukaemia. *Br. J. Haematol.* **125**, 601–604 (2004).
29. Zack, T. I. et al. Pan-cancer patterns of somatic copy number alteration. *Nat. Genet.* **45**, 1134–1140 (2013).
30. Baell, J. B. et al. Inhibitors of histone acetyltransferases KAT6A/B induce senescence and arrest tumour growth. *Nature* **560**, 253–257 (2018).
31. Sharma, S. et al. Targeting KAT6A/KAT6B dependencies in breast cancer with a novel selective, orally bioavailable KAT6 inhibitor, CTx-648/PF-9363. *Cell Chem. Biol.* **30**, 1191–1210.e20 (2023).
32. Mukohara, T. et al. Inhibition of lysine acetyltransferase KAT6 in ER(+)HER2(-) metastatic breast cancer: a phase 1 trial. *Nat. Med.* **30**, 2242–2250 (2024).
33. Arboleda, V. A. et al. De novo nonsense mutations in KAT6A, a lysine acetyltransferase gene, cause a syndrome including microcephaly and global developmental delay. *Am. J. Hum. Genet.* **96**, 498–506 (2015).
34. Tham, E. et al. Dominant mutations in KAT6A cause intellectual disability with recognizable syndromic features. *Am. J. Hum. Genet.* **96**, 507–513 (2015).
35. Clayton-Smith, J. et al. Whole-exome-sequencing identifies mutations in histone acetyltransferase gene KAT6B in individuals with the Say-Barber-Biesecker variant of Ohdo syndrome. *Am. J. Hum. Genet.* **89**, 675–681 (2011).
36. Simpson, M. A. et al. De novo mutations of the gene encoding the histone acetyltransferase KAT6B cause Genitopatellar syndrome. *Am. J. Hum. Genet.* **90**, 290–294 (2012).
37. Thomas, T., Voss, A. K., Chowdhury, K. & Gruss, P. Querkopf, a MYST family histone acetyltransferase, is required for normal cerebral cortex development. *Development* **127**, 2537–2548 (2000).
38. Kraft, M. et al. Disruption of the histone acetyltransferase MYST4 leads to a Noonan syndrome-like phenotype and hyperactivated MAPK signaling in humans and mice. *J. Clin. Investig.* **121**, 3479–3491 (2011).
39. Merson, T. D. et al. The transcriptional coactivator Querkopf controls adult neurogenesis. *J. Neurosci.* **26**, 11359–11370 (2006).
40. Bergamasco, M. I. et al. Loss of KAT6B causes premature ossification and promotes osteoblast differentiation during development. *Dev. Biol.* **520**, 141–154 (2025).
41. Bergamasco, M. I. et al. Increasing histone acetylation improves sociability and restores learning and memory in KAT6B-haploinsufficient mice. *J. Clin. Investig.* **134**, e167672 (2024).
42. Katsumoto, T. et al. MOZ is essential for maintenance of hematopoietic stem cells. *Genes Dev.* **20**, 1321–1330 (2006).
43. Thomas, T. et al. Monocytic leukemia zinc finger protein is essential for the development of long-term reconstituting hematopoietic stem cells. *Genes Dev.* **20**, 1175–1186 (2006).
44. Vanyai, H. K. et al. MOZ directs the distal-less homeobox gene expression program during craniofacial development. *Development* **146**, dev175042 (2019).
45. Vanyai, H. K., Thomas, T. & Voss, A. K. Mesodermal expression of Moz is necessary for cardiac septum development. *Dev. Biol.* **403**, 22–29 (2015).
46. Perez-Campo, F. M., Borrow, J., Kouskoff, V. & Lacaud, G. The histone acetyltransferase activity of monocytic leukemia zinc finger is critical for the proliferation of hematopoietic precursors. *Blood* **113**, 4866–4874 (2009).
47. Perez-Campo, F. M., Costa, G., Lie, A. L. M., Stifani, S., Kouskoff, V. & Lacaud, G. MOZ-mediated repression of p16(INK) (4) (a) is critical for the self-renewal of neural and hematopoietic stem cells. *Stem Cells* **32**, 1591–1601 (2014).
48. Sheikh, B. N. et al. MOZ (MYST3, KAT6A) inhibits senescence via the INK4A-ARF pathway. *Oncogene* **34**, 5807–5820 (2015).
49. Sheikh, B. N. et al. MOZ (KAT6A) is essential for the maintenance of classically defined adult hematopoietic stem cells. *Blood* **128**, 2307–2318 (2016).

50. Ikuta, K. & Weissman, I. L. Evidence that hematopoietic stem cells express mouse c-kit but do not depend on steel factor for their generation. *Proc. Natl. Acad. Sci. USA* **89**, 1502–1506 (1992).
51. Morrison, S. J., Hemmati, H. D., Wandycz, A. M. & Weissman, I. L. The purification and characterization of fetal liver hematopoietic stem cells. *Proc. Natl. Acad. Sci. USA* **92**, 10302–10306 (1995).
52. Kiel, M. J., Yilmaz, O. H., Iwashita, T., Yilmaz, O. H., Terhorst, C. & Morrison, S. J. SLAM family receptors distinguish hematopoietic stem and progenitor cells and reveal endothelial niches for stem cells. *Cell* **121**, 1109–1121 (2005).
53. Osawa, M., Hanada, K., Hamada, H. & Nakauchi, H. Long-term lymphohematopoietic reconstitution by a single CD34-low/negative hematopoietic stem cell. *Science* **273**, 242–245 (1996).
54. Sheikh, B. N. et al. MOZ and BMI1 play opposing roles during Hox gene activation in ES cells and in body segment identity specification in vivo. *Proc. Natl. Acad. Sci. USA* **112**, 5437–5442 (2015).
55. Sheikh, B. N., Metcalf, D., Voss, A. K. & Thomas, T. MOZ and BMI1 act synergistically to maintain hematopoietic stem cells. *Exp. Hematol.* **47**, 83–97.e88 (2017).
56. Geelen, J. A. Hypervitaminosis A induced teratogenesis. *CRC Crit. Rev. Toxicol.* **6**, 351–375 (1979).
57. Kessel, M. & Gruss, P. Homeotic transformations of murine vertebrae and concomitant alteration of Hox codes induced by retinoic acid. *Cell* **67**, 89–104 (1991).
58. van der Lugt, N. M. et al. Posterior transformation, neurological abnormalities, and severe hematopoietic defects in mice with a targeted deletion of the bmi-1 proto-oncogene. *Genes Dev.* **8**, 757–769 (1994).
59. van der Vlag, J. & Otte, A. P. Transcriptional repression mediated by the human polycomb-group protein EED involves histone deacetylation. *Nat. Genet.* **23**, 474–478 (1999).
60. Newman, D. M. et al. Acetylation of the Cd8 locus by KAT6A determines memory T cell diversity. *Cell Rep.* **16**, 3311–3321 (2016).
61. Lasko, L. M. et al. Discovery of a selective catalytic p300/CBP inhibitor that targets lineage-specific tumours. *Nature* **550**, 128–132 (2017).
62. Sommerhalder, D. H. E. et al. First-in-human phase 1 dose escalation study of the KAT6 inhibitor PF-07248144 in patients with advanced solid tumors. *J. Clin. Oncol.* **41**, 1054–1054 (2023).
63. Thomas, T., Loveland, K. L. & Voss, A. K. The genes coding for the MYST family histone acetyltransferases, Tip60 and Mof, are expressed at high levels during sperm development. *Gene Expr. Patterns* **7**, 657–665 (2007).
64. Liao, Y., Smyth, G. K. & Shi, W. The Subread aligner: fast, accurate and scalable read mapping by seed-and-vote. *Nucleic Acids Res.* **41**, e108 (2013).
65. Ritchie, M. E. et al. limma powers differential expression analyses for RNA-sequencing and microarray studies. *Nucleic Acids Res.* **43**, e47 (2015).
66. Robinson, M. D., McCarthy, D. J. & Smyth, G. K. edgeR: a Bioconductor package for differential expression analysis of digital gene expression data. *Bioinformatics* **26**, 139–140 (2010).
67. Leek, J. T. & Storey, J. D. Capturing heterogeneity in gene expression studies by surrogate variable analysis. *PLoS Genet.* **3**, 1724–1735 (2007).
68. Kaya-Okur, H. S. et al. CUT&Tag for efficient epigenomic profiling of small samples and single cells. *Nat. Commun.* **10**, 1930 (2019).
69. Wichmann, J. et al. Loss of TIP60 (KAT5) abolishes H2AZ lysine 7 acetylation and causes p53, INK4A, and ARF-independent cell cycle arrest. *Cell Death Dis.* **13**, 627 (2022).
70. Orlando, D. A. et al. Quantitative ChIP-Seq normalization reveals global modulation of the epigenome. *Cell Rep.* **9**, 1163–1170 (2014).
71. Liao, Y., Smyth, G. K. & Shi, W. The R package Rsubread is easier, faster, cheaper and better for alignment and quantification of RNA sequencing reads. *Nucleic Acids Res.* **47**, e47 (2019).
72. Ritchie, M. E. et al. Empirical array quality weights in the analysis of microarray data. *BMC Bioinform.* **7**, 261 (2006).
73. Law, C. W., Chen, Y., Shi, W. & Smyth, G. K. voom: precision weights unlock linear model analysis tools for RNA-seq read counts. *Genome Biol.* **15**, R29 (2014).
74. Liu, R. et al. Why weight? Modelling sample and observational level variability improves power in RNA-seq analyses. *Nucleic Acids Res.* **43**, e97 (2015).
75. Mah S. Y. Y. et al. ING4 and ING5 are essential for histone H3 lysine 14 acetylation and epicardial cell lineage development. *Development* **151**, dev202617 (2024).
76. Yang, Y. et al. The histone lysine acetyltransferase HBO1 (KAT7) regulates hematopoietic stem cell quiescence and self-renewal. *Blood* **139**, 845–858 (2022).

Acknowledgements

The authors would like to thank N. Blasch, L. Wilkins and K. Florides for excellent animal care; C. Burström for expert technical assistance; S. Wilcox, K. Weston, T. Nikolaou and the Walter and Eliza Hall Histology department for exceptional service. M.I.B. was supported by an Australian Government Postgraduate Award. This work was supported by the Australian National Health and Medical Research Council through Project Grant 1160517 to T.T., Ideas Grant 2010711 to T.T., Research Fellowships 1081421 to A.K.V. and 1154970 to G.K.S. and Investigator Grant 1176789 to A.K.V.; through the Independent Research Institutes Infrastructure Support Scheme; and by the Victorian Government through an Operational Infrastructure Support Grant.

Author contributions

M.I.B. and T.T. carried out experiments, performed data analyses and drafted the manuscript. Y.Y. and B.N.S. carried out experiments. A.L.G. performed the bioinformatics data analysis supervised by G.K.S. A.K.V. and T.T. conceived the project, designed experiments, performed data analyses and drafted the manuscript. All authors read and contributed to the manuscript.

Competing interests

The Thomas and Voss laboratories have received research funding from CTx CRC for work unrelated to this project. All other authors declare no competing interests.

Additional information

Supplementary information The online version contains supplementary material available at <https://doi.org/10.1038/s41467-025-57155-4>.

Correspondence and requests for materials should be addressed to Anne. K. Voss or Tim Thomas.

Peer review information *Nature Communications* thanks the anonymous reviewer(s) for their contribution to the peer review of this work. A peer review file is available.

Reprints and permissions information is available at <http://www.nature.com/reprints>

Publisher's note Springer Nature remains neutral with regard to jurisdictional claims in published maps and institutional affiliations.

Open Access This article is licensed under a Creative Commons Attribution 4.0 International License, which permits use, sharing, adaptation, distribution and reproduction in any medium or format, as long as you give appropriate credit to the original author(s) and the source, provide a link to the Creative Commons licence, and indicate if changes were made. The images or other third party material in this article are included in the article's Creative Commons licence, unless indicated otherwise in a credit line to the material. If material is not included in the article's Creative Commons licence and your intended use is not permitted by statutory regulation or exceeds the permitted use, you will need to obtain permission directly from the copyright holder. To view a copy of this licence, visit <http://creativecommons.org/licenses/by/4.0/>.

© The Author(s) 2025